

Unsteady Surface Pressures on the Space Launch System Block 1B Cargo Liftoff Configuration

Lee J. Mears*, Patrick R. Shea†, Jesse G. Collins‡, Morgan A. Walker‡, and Jeremy T. Pinier§

NASA Langley Research Center, Hampton, Virginia

Pourya Nikoueeayan¶, Marvin Perry¶, John Strike††, Benjamin Wimpenny††, and Michael D. Hind††

Resono Pressure Systems, Inc., Laramie, Wyoming

Jonathan W. Naughton**

University of Wyoming, Laramie, Wyoming

A 1.75%-scale model of the NASA Space Launch System Block 1B Cargo vehicle was tested at the NASA Langley Research Center 14- by 22-Foot Subsonic Tunnel. These experiments provided a test bed for validating unsteady surface pressure measurements acquired via lengths of pressure tubing and an ESP pressure scanner. Pressure was measured using an azimuthal array of pressure taps located on the nose of the Block 1B Cargo vehicle. Unique flow physics were observed in the wind tunnel test, especially the interaction between the launch vehicle and the support tower, which produced strong oscillations that were absent in the vehicle-alone configuration. It is suspected that a wake interaction produced a resonant flow response when the tower is immediately downstream of the vehicle, and coherent pressure fluctuations were observed at all pressure taps in the azimuthal array.

Nomenclature

D	SLS core diameter, ft
h	Launch vehicle elevation above launch platform, ft
h/L	Nondimensional launch vehicle elevation above launch platform
L	Launch tower height, ft
M_∞	Freestream Mach number
p_{rms}	Root-mean-squared fluctuating pressure, psf
q_∞	Freestream dynamic pressure, psf
r	Correlation coefficient
Re_D	Reynolds number based on core diameter
St_D	Strouhal number based on core diameter
ψ_{azm}	Azimuthal angle on model surface, degrees
θ	Pressure port angle, degrees
γ^2	Magnitude-squared coherence
σ	Nondimensional fluctuating pressure, p_{rms}/q_∞
CUI	Controlled Unclassified Information
ESP	Electronic pressure scanner

*Research Engineer, Configuration Aerodynamics Branch, AIAA Member ✉ lee.j.mears@nasa.gov

†Research Engineer, Configuration Aerodynamics Branch, AIAA Senior Member

‡Research Engineer, Configuration Aerodynamics Branch, AIAA Member

§Research Engineer, Configuration Aerodynamics Branch, AIAA Associate Fellow

¶Chief Technology Officer, AIAA Member

|| Systems Engineer, AIAA Member

†† Staff Engineer, AIAA Member

**Professor, Mechanical Engineering Department, AIAA Associate Fellow

FRF	Frequency response function
ML-2	Mobile Launch tower for SLS Block 1B
PSD	Power spectral density, psi^2/Hz
SLS	Space Launch System
SNR	Signal to Noise Ratio

I. Introduction

Ground-wind effects produce separated flow dynamics on slender, upright launch vehicles and complex wake interactions with the launch tower. Avoiding destructive aeroelastic effects prior to launch and ensuring tower clearance during liftoff are critical to mission success, which requires extensive characterization of the flow environment. Improved understanding of the flow physics created by the vehicle and launch tower is essential for predicting the vehicle response in the ground-wind loads environment, which has been historically studied at the NASA Langley Research Center since the Apollo program [1]. These studies applied the knowledge gained from fundamental experiments in high-Reynolds-number cylinder flows by Roshko [2] and Achenbach [3] to the problem of surface winds acting on the Saturn V while on the launch pad. The aeroelastic effects of this rocket were essentially unknown during the design phase, and they posed substantial risk to manned space missions to the moon until sufficient testing was conducted [4]. The challenge of ground-wind loads has not substantially changed in the last 50 years, but improved design and research tools are available to define risk and operational envelopes for the next generation of rockets to leave Earth's orbit.

The NASA Space Launch System (SLS) is a heavy-lift launch vehicle designed for the next manned lunar missions and supporting the first human exploration of Mars (Fig. 1). Extensive wind tunnel testing has been completed for Block 1 Crew and Cargo configurations of the launch vehicle, including measurements of forces, moments, and surface pressure [5–7]. Wind tunnel tests and numerical simulations encompass the entire regime of flight Mach numbers to define aerodynamic loading, including the liftoff configuration to assess ground-wind loads. The present wind tunnel test in the 14- by 22-Foot Subsonic Tunnel provided the force and moments for the larger Block 1B Crew and Cargo vehicles with and without the newly designed Mobile Launch tower (ML-2). The test focused on building a database for steady loads at incompressible conditions that the vehicle will experience on the launch pad. This also presented an opportunity to acquire unsteady surface pressure data without significant additional investment in sensors or model alterations by leveraging a nonreimbursable Space Act Agreement between NASA and the University of Wyoming.

A separate paper (Ref. [9]) will furnish a detailed assessment of the new measurement technique, and only a few details will be presented here. This test is unique in that unsteady pressure is measured using static taps designed for time-averaged pressure rather than using transducers mounted directly on the model surface. Individual pressure taps are connected to a remote ESP (electronic pressure scanner) module via lengths of flexible tubing [10, 11]. This methodology leads to potential cost-savings over discrete sensors at the expense of additional data processing to remove the influence of the pressure tubes – namely signal attenuation, lag, and resonance [12]. The results can be improved for empirically determined inverse transfer functions by using a Wiener filter to reduce the impact of high-frequency noise on the reconstruction [13].

Postprocessing included a combination of analytical and empirical system characterization, which has previously been applied to experiments on wind tunnel blades and shock tubes [14–16]. Pressure fluctuations were recorded using an ESP acquisition system provided by Resono, and validation was performed using simultaneously acquired high-fidelity piezoresistive pressure sensors (Kulites) mounted on the surface of the wind tunnel model close to the pressure taps. The selection of Kulites was not ideal because of the high pressure range (15 psi), but provided adequate validation in cases with strong pressure fluctuations and high signal-to-noise ratio (SNR). The validation study calculated a Frequency Response Function (FRF) and concluded that the reconstructed ESP signals remained within 1 dB of gain magnitude and 10° of phase of the neighboring Kulite up to 500 Hz and are thus an accurate representation of the surface pressure fluctuations on the model below 500 Hz [17].

The present paper examines the flow physics observed in the wind tunnel test using this measurement methodology. A slender launch vehicle mounted vertically on a launch pad approximates a circular cylinder in crossflow, which is one of the classical problems in fluid mechanics with ubiquitous practical applications in engineering [18]. Extending our understanding of a single, rigidly mounted, two-dimensional cylinder to a realistic launch vehicle with protuberances, finite length, and multiple body interactions is not straightforward; however, several key insights provide a helpful understanding of the flow physics. In the following discussion, the nomenclature of Szechenyi (Ref. [19]) is used, and the Reynolds number ranges given are for smooth cylinders. The Reynolds number defined by the cylinder diameter

(Re_D) is the parameter that most influences the dynamical behavior of the flow, and defines the following three broad regimes: *subcritical* flow ($Re_D < 2 \times 10^5$), *transcritical* flow ($2 \times 10^5 < Re_D < 6 \times 10^6$), and *supercritical* flow ($Re_D > 6 \times 10^6$). The most prominent feature of both subcritical and supercritical cylinder flows is vortex shedding present in the wake, which produces oscillating pressure forces at Strouhal numbers defined by the cylinder diameter and incoming flow velocity (St_D) around 0.2 in subcritical flows and 0.26 - 0.30 in supercritical flows. No harmonic vortex shedding is observed in the transcritical flow regime, and instead, the wake is characterized by broadband pressure fluctuations. These approximate ranges vary significantly when surface roughness is applied to the cylinder, which transitions the laminar boundary layer on the cylinder surface to a turbulent boundary layer and lowers the Re_D numbers associated with the transcritical and supercritical flow regimes. Additional end effects from the finite cylinder length extend several diameters away, and depending on the specific end condition (e.g., flat or rounded), can dramatically change the flow behavior several cylinder diameters away from the tip [19].

The flow physics become substantially more complicated in cases when an additional bluff body interacts with the flowfield, such as the launch tower and rocket boosters attached to the vehicle core. The parameter space required for defining the geometry increases substantially with the addition of spacing, relative wind angle, and relative size of the two bodies, all of which strongly influence the flow physics. To better understand the flow environment in the wind tunnel test, higher overall fidelity of data collection was accomplished by including unsteady pressure measurements. High intensity pressure fluctuations indicate regions with separated flow, while correlation of pressure signals indicates coupled flow physics at different parts of the cylinder. Spectral analysis identifies specific frequencies related to oscillating pressure, which can then be examined for spatial coherence, as well. This analysis leads to greater understanding of the aerodynamic environment experienced by the SLS Block 1B Cargo vehicle, particularly related to wake interactions with the ML-2 tower.

II. Experimental Methodology

The experiment was performed at the NASA Langley Research Center in the 14- by 22-Foot Subsonic Tunnel (14x22). This closed-circuit, atmospheric-pressure wind tunnel is capable of operating in different test-section configurations, and all present tests were conducted using the closed test section walls. With the walls closed, the test section dimensions are 14.5 ft high by 21.75 ft wide by 50 ft long. The flow in the settling chamber is conditioned by a flow-straightening honeycomb, four square-mesh screens with a mesh count of 10 per inch and 64% open area, and a tunnel contraction area of 9 to 1. Previous studies have reported turbulence intensities between 0.05-0.07% of the freestream velocity at a dynamic pressure (q_∞) of 50 psf [20].

The runs were acquired using point-pause motion of the test article. Once pressure readings and force and moment readings have settled at a specified dynamic pressure and vehicle orientation, acquisition is initiated. Temperature variations resulted in a range of Mach and Reynolds numbers during testing. For nominal $q_\infty = 50$ psf tests, the Mach number varied between 0.1846 and 0.1871. The dynamic pressure typically varies by 0.3% during data acquisition. Variations in outdoor temperature resulted in test section temperatures from 70°F to 105°F, with Reynolds number defined by the core diameter (Re_D) ranging between 5.3×10^5 and 6.0×10^5 .

A. SLS Block 1B Cargo Model

Although the model details and test data are Controlled Unclassified Information (CUI), the limited unsteady pressure data used for the technology demonstration described in this paper have been deemed Fundamental Research and are not subject to Export Control. The location of the pressure taps is considered sensitive information and will not be included. Other details required to interpret the pressure data and the fluid mechanics phenomena have been included.

The 1.75%-scale model consists of two primary components: a centerbody core with an attached pair of solid rocket boosters (SRBs) – together comprising the SLS Block 1B Cargo launch vehicle – and a mobile launch tower (ML-2) that provides support to the vehicle prior to liftoff. The launch vehicle with the ML-2 is pictured in Fig. 2. Distributed roughness (#80 grit carborundum) is adhered to the entire vehicle surface to promote transition to turbulence. The impact of the grit application on unsteady pressure is not known, since tests were not repeated for a clean model. The movable umbilicals that interface with the launch vehicle have been painted red (shown here in the retracted configuration), while the tower structure is painted black. The gap between the vehicle and the closest face of the ML-2 is approximately 1.28 core diameters (D). The current effort focuses on a single azimuthal array of pressure taps on the vehicle centerbody away from the SRBs; the approximate location of this array is shown with a cyan band in Fig. 2.

B. Model Configurations

Three sequences of testing were conducted, each consisting of similar flow conditions with changes to the model configuration, shown in Fig. 3. The vehicle configurations are as follows: C1, with the Mobile Launch tower and umbilicals retracted, (Fig. 3(a)); C2, with the Mobile Launch tower and umbilicals deployed (Fig. 3(b)); and C3, with the Mobile Launch tower removed (Fig. 3(c)). Umbilicals are five support structures connecting the ML-2 and the launch vehicle that fall away from the vehicle shortly before liftoff, which are shown in red in Fig. 3(a) and (b). Deployment of the umbilicals simply means that the parts are moved away from the tower and are positioned very close to the vehicle surface – in reality, the umbilicals attach to the launch vehicle, but for purposes of force and moment testing, a small clearance gap is maintained between the parts. The ML-2 was completely removed from the ground plane for configuration C3, as shown in Fig. 3(c).

The vehicle is mounted on a sting with motorized height adjustment relative to the launch tower and tests were conducted at nominal height increments of $h/L = 0.1$ over a range of $h/L = -0.003$ to 0.876 , where h equals the vertical elevation of the vehicle above the ML-2 and L is the height of the launch tower, as shown in Fig. 4. Due to the selected reference point on the vehicle, $h/L = -0.003$ is the lowest height tested, where the SLS vehicle remains prior to liftoff.

The vehicle and launch tower are mounted on a yaw table in the liftoff configuration perpendicular to the wind tunnel floor. In this configuration, the vehicle's angle of attack is 90° and the freestream flow simulates incoming ground winds. Figure 5 shows the definition of wind direction, ψ_{azm} , ranging from 0° to 360° with respect to the vehicle and ML-2. The cardinal directions correspond to the geographical orientation of Launch Pad 39-B in Cape Canaveral, Florida, where the ML-2 lies directly north of the SLS vehicle. Tests were conducted using ψ_{azm} increments of 10° , resulting in 33 angles, since 80° , 90° , and 100° were unattainable (gray region in Fig. 5) due to mechanical constraints of the yaw table.

C. Unsteady Pressure Measurements

The pressure scanner used was a TE Connectivity ESP-32HD module with a full scale range of 1 psid. 12 of the 32 available pressure scanner ports were connected to pressure taps on the model surface in an azimuthal ring (blue circles in Fig. 6) at a single axial location on the model. The tubing length was approximately 14 inches total, comprising 6 inches of stainless steel tubing, 8 inches of 0.040 inch inner diameter Tygon tubing, and an adapter to a short length (about 1/4 inch) of 0.065 inch inner diameter tubing to connect to the ESP module. Although the pressure ports are located above the SRBs, as shown in Fig. 2, the outline of the SRBs are shown in Fig. 6 for reference. The pressure ports are sequentially numbered from 1 to 12, and Ports 1, 4, 9, 10, and 11 have corresponding comparison Kulites (yellow triangles in Fig. 6). The data from each pressure port will be plotted with respect to the incoming flow direction, ψ_{azm} , using a new variable, θ , shown in Fig. 6). Port position will be oriented such that the nominal stagnation point will be at $\theta = 0^\circ$, and positive θ in the clockwise direction looking top-down to the model.

The ESP sampling rate for each channel is 2,000 Hz for a duration of 6 seconds, resulting in 12,000 total samples. Since the signal is digitally multiplexed, no antialiasing filtering is applied during digitization. The ESP module does not sample individual channels simultaneously; instead, each subsequent port is sampled at $40 \mu s$ intervals within the $500 \mu s$ sampling period.

III. Data Reduction

A. Pressure Reconstruction

The reconstruction of pneumatically distorted pressure fluctuations at the model surface follows the theory developed by Bergh and Tjeldeman [21] and a Wiener deconvolution algorithm developed by Whitmore and Wilson [13]. The length of pressure tubing is modeled as a system of acoustic ducts with an associated transfer function that describes how pressure fluctuations applied at the surface of the model are measured by the ESP module at the end of the tube. The temperature and pressure measured during wind tunnel runs are used to update the sonic velocity and dynamic viscosity used by the inverse transfer function for each unsteady pressure acquisition, but changes in humidity were not considered. Frequency response functions are calculated and show that the reconstructed ESP match the validation Kulites within 1 dB of magnitude and 10° of phase response up to 500 Hz [17]. The methodology has been applied to previous wind tunnel tests by Resono; additional details on these efforts appear in Refs. [15, 16].

B. Analysis Methods

Unsteady pressure measurements permit higher fidelity data analysis than time-averaged data, and this is accomplished in the present test using a combination of statistical and spectral analysis methods. The pressure intensity, σ , is calculated by computing the root-mean-square of each mean-subtracted time series and nondimensionalized by the dynamic pressure for that run. Correlation coefficients, r , are calculated from the each simultaneously acquired time series with respect to a single reference port. Typical spectra for ESP measurements are calculated using Welch's periodogram method with averaging block sizes of 400 samples, resulting in frequency resolution of 5 Hz and a total number of 30 averages with Hanning windowing. The same averaging approach is used to calculate the magnitude-squared coherence, γ^2 , between each sensor and the selected reference port.

IV. Results and Discussion

The pressure fluctuations on the surface of the vehicle provide valuable insight into the flow physics observed in the wind tunnel test. As mentioned previously, a new variable, θ , is introduced to display the surface pressure with respect to the incoming flow direction such that $\theta = 0^\circ$ always corresponds with the stagnation point of the flow, assuming the vehicle is a circular cylinder (see Fig. 6). This permits a more intuitive comparison when examining the flow physics at different incoming flow angles, since the nominal stagnation point defined by the incoming flow direction is always "clocked" to $\theta = 0^\circ$. In addition to variations in ψ_{azm} and h/L , the flowfield differences at three vehicle and ML-2 configurations (C1, C2, and C3) will be examined as well (see Fig. 3).

A. Pressure Intensity (σ)

The overall fluctuation intensity at each measurement location can be displayed as a 2-D contour plot with the incoming flow angle, ψ_{azm} , plotted on the abscissa and pressure sensor location, θ , on the ordinate axis. Each figure contains data from 33 separate data acquisition test points as the model is rotated through a sweep of ψ_{azm} . As noted previously, flow angles from 80° to 100° were not measured due to mechanical constraints, and these angles are hashed out in the figures. Plotting is limited ("clipped") to $\sigma = 0.25$ in order to provide a visually distinctive range and facilitate useful comparisons to cases with weaker unsteadiness. Any clipping in the figure is noted with a black triangle; the maximum level observed in the test was $\sigma = 0.27$. Figure 7 shows the distribution of pressure intensity at $h/L = -0.003$ for C1, where the launch vehicle sits at the ground plane. The strongest pressure fluctuations are noted at $\psi_{azm} = 180^\circ$, where the ML-2 is immediately downstream of the vehicle. These peaks are located at $\theta = \pm 90^\circ$, close to where separation would be expected on the sides of the vehicle [22]. A region of very low pressure fluctuations occurs at $\theta = 0^\circ$, near the stagnation point of the flow. An additional region of relatively high pressure intensity is observed near $\theta = -120^\circ$ at $\psi_{azm} = 330^\circ$, where shedding from the tower is the likely source of relatively high unsteadiness on the surface of the vehicle. Near $\psi_{azm} = 0^\circ$, unsteadiness is very low for all pressure ports because the flow passes through the ML-2 tower before reaching the vehicle, effectively reducing the fluctuations in the flowfield.

The next figures show the change in σ with increasing vertical elevation of the vehicle relative to the height of the tower, h/L . As h/L is increased from -0.003 to 0.1 , the pressure fluctuations reduce significantly, as shown in Fig. 8. Some unsteadiness is observed at $\psi_{azm} = 180^\circ$ and $\theta = \pm 90^\circ$, as well as $\psi_{azm} = 320$ - 330° , but at less than half the intensity observed at $h/L = -0.003$. The results at $h/L = 0.2$ (Fig. 9) appear very similar to $h/L = 0.1$, but with increased pressure fluctuations at $\psi_{azm} = 330^\circ$. Pressure fluctuations increase at $h/L = 0.3$ (Fig. 10), especially at $\psi_{azm} = 0^\circ$ where the tower is upstream of the vehicle, because at this height, the shear layer produced by the flow over the top of the tower impinges near the axial location of the pressure sensors. Figure 11 shows that the magnitude of pressure fluctuations observed at $h/L = 0.4$ is similar to $h/L = 0.2$ (Fig. 9) and much lower than $h/L = 0.3$ (Fig. 10). At vehicle heights of $h/L = 0.5$ (Fig. 12) and above, the influence of the tower becomes negligible at the measurement locations and the results appear similar to those of C3 (no tower), with low unsteadiness except at $\theta = \pm 90^\circ$. The highest pressure fluctuation intensities centered around $\theta = \pm 90^\circ$ indicate that flow separation occurs near the angle typical of supercritical cylinder flow ($\sim 95^\circ$) instead of transcritical flow ($\sim 110^\circ$) [19]. At the maximum height, $h/L = 0.876$ (Fig. 13), unsteadiness is observed at $\psi_{azm} = 300^\circ$, and although the vehicle is nearly clear of the launch tower (and the pressure port array is far outside direct influence of the tower), this seems to be an effect from the tower and is not observed in the C3 cases. Since the ML-2 is not present in C3, negligible differences in σ are observed with variation in h/L . Thus, the distributions in σ for C3 at $h/L = -0.003$ and $h/L = 0.876$ (Fig. 14 and Fig. 15) are nearly identical.

Figure 16 shows the pressure intensity for C2, which has umbilicals deployed between the ML-2 and the SLS vehicle. The overall distribution of σ is very similar to C1 at $h/L = -0.003$ (Fig. 7). The strongest fluctuations appear at ψ_{azm}

= 180° , but overall intensity is reduced compared to C1, indicating that the wake interaction associated with highest unsteadiness is disrupted by the presence of the deployed umbilicals in the gap between the vehicle and tower.

B. Correlation Coefficients (r)

Another important quantity of interest is the strength of the linear relationship between the time history of two signals, which indicates whether the sensors are experiencing pressure fluctuations at the same points in time, even if the fluctuations are not periodic. This is accomplished by calculating the correlation coefficient between a reference sensor and another simultaneously acquired pressure measurement. A correlation coefficient value of 1 means that the two sensors are essentially reading identical signals, although there may be significant differences in amplitude. A correlation coefficient value of -1 means that two sensors are reading inverted signals, i.e., one is reading a positive fluctuation in pressure while the other is reading a negative one. Finally, a correlation coefficient value near 0 means that the two sensors are reading signals that are evidently unrelated. Mapping the correlation coefficient for all ports provides a qualitative snapshot of the relationship between pressure fluctuations on the model and identifies organized flow features on the model surface.

Since the strongest pressure fluctuations occur near $\theta = \pm 90^\circ$, where apparent flow separation occurs, the reference probe location is set to $\theta = 90^\circ$. In Fig. 17, the pressure signals are all correlated to the reference point for a range of incoming flow directions, ψ_{azm} , for C1 at $h/L = -0.003$. When ψ_{azm} is near 0° , the tower blocks the incoming flow and there is very little correlation in the signals because the flow is disorganized in the wake of the tower. At higher values of ψ_{azm} , large swaths of positively correlated pressure fluctuations appear on both sides of the vehicle, while the stagnation point centered near $\theta = 0^\circ$ remains uncorrelated, which is expected because the unsteadiness is minimal here. When the tower is directly downstream of the vehicle ($\psi_{azm} = 180^\circ$), where the strongest pressure fluctuations occur, negatively correlated pressure is observed between $\theta = -15^\circ$ and -165° . Even though the intensity of pressure fluctuations at $\pm 30^\circ$ is not as strong as $\pm 90^\circ$ (Fig. 7), the out of phase behavior is still observed in this upstream region. This could be caused by strong pressure disturbances transmitted from the downstream separated flow to the upstream region where the boundary layer remains attached. The narrow range where this behavior is observed, between $\psi_{azm} = 170^\circ$ and 190° , suggests that a resonant flow mechanism in the vehicle wake interaction with the tower is responsible for the alternating unsteady pressure measured at this orientation.

As ψ_{azm} is increased to 210° through 240° , the only significant correlation occurs near the reference line, indicating that the flow physics generating unsteady pressure here are not significantly felt elsewhere on the vehicle. As ψ_{azm} approaches 270° , where the reference sensor is immediately between the vehicle and tower, the signals are positively correlated with fluctuations at a broad range of θ except near the stagnation region, such that nearly the full azimuthal ring of sensors are recording related pressure unsteadiness. Another interesting detail observed at $\psi_{azm} = 270^\circ$ is that the stagnation point, indicated by a region of near zero correlation, migrates closer to $\theta = -30^\circ$ rather than the nominal θ value of 0° .

Differences between the two configurations with the ML-2 installed, C1 (umbilicals retracted) and C2 (umbilicals deployed), are minor with respect to the correlation of pressure signals shown in Fig. 18. A slightly stronger negative correlation coefficient is observed at $\psi_{azm} = 180^\circ$, but the large-scale flow physics are not significantly affected by the presence of additional blockage within the gap between the vehicle and launch tower. The C3 configuration, where the ML-2 is removed (Fig. 19), shows a marked difference from C1 and C2, with no regions displaying significant negative correlation. This means that there are no out of phase pressure fluctuations related to flow separation on the opposite side of the vehicle, and instead, the fluctuations are mostly in phase throughout the range of ψ_{azm} . An exception is observed between $\psi_{azm} = 270^\circ$ and 315° , but the cause for this is not immediately clear and may be attributed to the strong asymmetry in the model geometry. The correlation map for C3 can be compared to C1 at maximum h/L in Fig. 20, which also shows the same region of slightly negatively correlated signals between $\psi_{azm} = 270^\circ$ and 315° . The pattern can be attributed to influence of the top of the SRBs, which are relatively far from the part of the vehicle where pressure measurements are made but are nonetheless the largest asymmetric aspect of the launch vehicle. No characteristic negative correlation related to alternating vortex shedding appears to be present in the cases without the tower. The next section will examine the Power Spectral Density (PSD) for specific cases of interest identified by strong pressure intensity, σ , to observe the frequency distribution.

C. Power Spectral Density (PSD)

Identifying how pressure fluctuations are distributed by frequency can provide important information on the flow physics present for different model orientations and configurations. Peaks in spectral energy are clearly observed in

Fig. 21, which shows the spatial distribution of surface pressure fluctuations at each frequency for the C1 configuration with highest pressure fluctuations at $\psi_{azm} = 180^\circ$ and $h/L = -0.003$. The bright yellow region at 22.5 Hz wraps around the circumference of the model (from -180° to $+180^\circ$) and is especially strong at $\pm 90^\circ$. Minimal fluctuations across all frequencies occur at the flow stagnation point, near $\theta = 0^\circ$, and attached flow on the surface of the model produces low energy within high-frequency regions (above 100 Hz) between $\theta = \pm 90^\circ$ centered at 0° . The broadband distribution on the leeside of the vehicle, between $\theta = \pm 120^\circ$ wrapping around the top and bottom of the figure, indicates fully separated flow between the vehicle and tower.

The same flow conditions are tested for C2, shown in Fig. 22, which includes the deployed umbilicals between the ML-2 and launch vehicle. The peak frequency increases to 27.5 Hz and overall intensity is lower than observed in C1, and apparent harmonics are also visible around 55 Hz and 82.5 Hz. Both configurations can be compared to experiments with only the launch vehicle (Fig. 23), with similar distribution in frequency to C1 and C2. Strong fluctuations at $\theta = \pm 90^\circ$ indicate the onset of separation; fully separated flow behind the vehicle produces a broad distribution of frequencies up to the maximum resolvable frequency, 1 kHz. The most significant difference between the cases with and without the tower present is that no peak frequencies appear without the tower, suggesting that the strong fluctuations are a coupled effect created by a wake interaction between the vehicle and tower. It is not clear how the wake interaction, which occurs in the gap between the vehicle and tower, produces pressure fluctuations that are apparent in the attached flow at the front of the vehicle, between $\theta = \pm 60^\circ$. Another case of interest is C1 at $\psi_{azm} = 270^\circ$, where the tower and vehicle are parallel to the incoming flow. Although significantly lower in magnitude than at $\psi_{azm} = 180^\circ$, the PSD in Fig. 24 shows a defined peak around 35 Hz that is also apparent at all values of θ .

The complex flowfield that exists in the wake interaction between two generic bluff bodies is difficult to predict from a fundamental physics perspective, let alone for complex geometries such as a cylindrical launch vehicle with protuberances and a semiporous truss structure. The PSD without the tower (Fig. 23) shows no coherent vortex shedding at any particular frequency when $\psi_{azm} = 180^\circ$ when the two SRBs are parallel to the flow. When the vehicle is rotated such that $\psi_{azm} = 270^\circ$ (Fig. 25), where the SRBs are now fore and aft of the vehicle, unsteadiness at approximately 35 Hz becomes apparent. The increase and tonal nature of the fluctuating pressure observed with blockage in the wake of the vehicle (Figs. 21 and 22) is a potential indication of resonant flow features occurring in the gap between two bodies, albeit at lower frequencies and at smaller gap spacings than observed in tandem cylinder studies in the subcritical flow regime, Re_D less than 2×10^5 [23]. The Strouhal number of the 22.5 Hz peak in Fig. 21 using the cylinder diameter D (St_D) equals 0.051, while the Strouhal number using the gap between the vehicle and the tower is 1.28 times higher (0.066) - neither of which appear physically meaningful in single or tandem cylinder flow studies. Treating the gap as a cavity and estimating Rossiter tones for the gap geometry yields expected frequencies in excess of 100 Hz [24], much higher than the fundamental frequencies observed. It is possible that separated shear layer excitation and acoustic resonance from the wake interaction with the tower are responsible for the strong pressure fluctuations that are felt upstream of flow separation on the vehicle surface, but the current measurements do not provide conclusive evidence of the underlying flow phenomena. Although surface pressure measurements are not sufficient for definitive characterization of the flow physics, additional off-body flowfield measurements are required to determine the mechanism driving the amplification in unsteady pressure.

D. Magnitude-squared Coherence (γ^2)

Similar to the correlation coefficients discussed in Section IV.B, the coherence between two signals is a measure of the linear dependency by testing for similar frequency components. While correlation can show which regions of the flowfield are fluctuating together (in phase or out of phase), coherence helps to understand whether the association between two signals is related to a specific frequency of interest. A magnitude-squared coherence (γ^2) value of 1 at any frequency indicates perfect agreement between signals at that frequency and implies strong similarity in the physical mechanism producing the pressure fluctuations, while a coherence value of zero indicates no relationship between the signals. The reference signal for Fig. 26 is at $\theta = 90^\circ$. The strong signal observed in the PSD at 22.5 Hz shows up on the entire range of θ values, although very weakly at the stagnation point near $\theta = 0^\circ$ and the sensor immediately between the vehicle and the tower at $\theta = 180^\circ$. Significant coherence is also observed at $\theta = 30^\circ$ through 150° for frequencies from 5 to 100 Hz that are notably absent on the other side of the vehicle, which implies that the broadband pressure fluctuations on each side of the vehicle are independent. Thus, it is likely that the strong negative correlation observed in Fig. 17 at $\psi_{azm} = 180^\circ$ is focused entirely on the unsteadiness at 22.5 Hz.

The broadband pressure fluctuations are coherent across all values of θ in Fig. 27 for $\psi_{azm} = 270^\circ$. In addition, the peak at 35 Hz produces discernible levels of coherence at all the pressure ports on the vehicle. The stagnation

point, which appeared to shift from 0° to -30° due to the presence of the launch tower, shows nearly zero coherence for the lower frequency pressure fluctuations yet the coherence at 35 Hz remains significant. This is indicative of a kind of resonant fluid mechanism that permits pressure disturbances to travel even toward the quietest region in the flowfield. Figure 28 shows the coherence plot for C2 at $\psi_{azm} = 180^\circ$. As observed in the PSD, the only obvious effect is that the primary frequency that is present across all values of θ is increased from 22.5 Hz to 27.5 Hz. The prevalence of coherent pressure signals at all azimuthal pressure taps indicates a resonant flow interaction with the tower with a fundamental frequency that is dependent on the tower orientation with respect to incoming flow direction and even the presence of deployed umbilicals.

Figure 29 shows very little coherence at θ greater than 30° away from the reference sensor at $\theta = 90^\circ$. Although it is likely from the peak in PSD at $\theta = 90^\circ$ that separation occurs here, widespread coherent fluctuations are not associated with the measurements at this point. Two additional reference locations are plotted for this case. When the stagnation point, $\theta = 0^\circ$, is used as the reference sensor in Fig. 30, the only notable coherence is widespread across all values of θ for frequencies from 15 Hz to 50 Hz, as well as a localized region at from $\theta = \pm 60^\circ$ consisting of higher frequency fluctuations, from 100 to 500 Hz. The last reference point is at $\theta = 180^\circ$ in Fig. 31, which reveals that coherence of low frequency pressure fluctuations below 40 Hz are widespread except at the stagnation point. Any higher frequency fluctuations observed in the fully separated wake behind the vehicle appear completely uncorrelated with the pressure measured at this region. Although coherence can provide strong evidence of the relationships between physical mechanisms driving the pressure fluctuations on the model surface, in this case, it shows that vortex shedding is absent in the vehicle-only configuration. Despite the geometrical similarity to a two-dimensional cylinder, the proximity to the tip of the launch vehicle and even asymmetrical influence of the SRBs can disrupt any coherent shedding.

E. High Resolution Case

A single case was selected for additional analysis specifically for unsteady pressure in the C3 configuration, with the vehicle alone at a height of $h/L = 0.5$, which is approximately the center of the wind tunnel. While typical increments in ψ_{azm} were 10° , this test consisted of rotation increments of 1° from $\psi_{azm} = 245^\circ$ to 275° . The underlying assumption was that this could approximate a higher spatial resolution measurement, assuming that overall flow physics are not substantially different throughout the range of rotation. This requires that the measurement region is largely axisymmetric (ignoring SRB and protuberance effects). Although this assumption is not entirely correct, the geometry is predominantly cylindrical and the data are shown at 1° increments in θ . This results in some small discontinuities, which can be seen in the plot of pressure intensity in Fig. 32.

The pressure intensity σ centers around a minimum point at $\theta = 0^\circ$. There is a smooth increase in pressure unsteadiness leading to sharp peaks very close to $\pm 90^\circ$, where the boundary layer separates. This is consistent with previous studies with rough cylinders in the transcritical Reynolds number range [22]. The two peaks are not symmetric, with greater unsteadiness noted at $\theta = -90^\circ$ than $+90^\circ$. This can be attributed to geometrical asymmetries on the SRB noses or other small protuberances on the vehicle core, or potentially to differences in grit application in the region. This can be compared to the pressure intensity plotted in Fig. 14, which is from a separate wind tunnel run and demonstrates consistent results. After the peak σ , the unsteadiness quickly falls to about half the peak amplitude on the rear of the vehicle, where the flow is fully separated. The pressure intensity associated with the separated flow is not fully converged with 6 seconds of acquisition, leading to the choppy appearance of the distribution of σ .

The PSD for this high spatial resolution case is plotted in Fig. 33. The highest amplitude signals, observed just above $\pm 90^\circ$, include slight peaks near 32.5 Hz, which is equal to $St_D = 0.075$. The increased spatial resolution does not help determine how this fundamental frequency might be relevant to the global flow dynamics experienced by the vehicle, but it does highlight how sharp the transitions from attached boundary layer with steadily increasing frequencies to fully separated flow, which encompasses pressure fluctuations up to the maximum resolvable frequency, 1 kHz. Although this additional test with small rotations does not reveal any unexpected features in the flowfield, it highlights how fortuitous the initial measurements were to capture the high unsteadiness at $\theta = \pm 90^\circ$; if the sensors were shifted by 5° in the original placement, this peak in unsteadiness would have been missed.

V. Conclusions

The current study investigated unsteady pressure at a single axial location on the core of the SLS Block 1B Cargo launch vehicle in three distinct configurations. Unsteady pressure measurements were conducted with variations in incoming flow direction (ψ_{azm}) and relative elevation of the launch vehicle with respect to the ML-2 launch tower

(h/L). Alternating pressure loading is observed when the tower is present and downstream of the vehicle at frequencies near 25 Hz, but in the vehicle-only configuration, alternating vortex shedding at distinct frequencies was not observed in the pressure measurements. Flow separation occurs near the angle typical of supercritical cylinder flow ($\sim 95^\circ$) instead of transcritical flow ($\sim 110^\circ$), as evidenced by the highest pressure fluctuation intensities centered around $\theta = \pm 90^\circ$. When the launch tower and vehicle are parallel to the incoming flow ($\psi_{azm} = 270^\circ$), the stagnation point shifts toward $\theta = -30^\circ$ on the core surface and a coherent pressure fluctuation becomes apparent at a higher frequency of 35 Hz.

The strong oscillations observed at $\psi_{azm} = 180^\circ$ for cases with the launch tower immediately downstream of the vehicle point to complex flow physics that are absent in the vehicle-alone flowfield. The interaction of the vehicle wake with the tower shows resonant flow characteristics, such as coherent fluctuations, and these measurements can help guide future studies to better understand the dynamical behavior of the flow structures present in the gap between the cylindrical vehicle and the truss-like tower. Additionally, umbilical systems connecting the tower and launch vehicle appear to disrupt strong fluctuations and increase the fundamental frequency slightly. As h/L increases, the magnitude of pressure fluctuations quickly decreases and by $h/L = 0.5$, the pressure forces acting at this vehicle location are nearly identical to the measurements of the vehicle alone. These observations will be useful in interpreting force and moment measurements made in the present wind tunnel test and determining the applicability of the observed flow patterns to the liftoff environment of the full-scale SLS vehicle.

Acknowledgments

This material is based upon work supported by the National Aeronautics and Space Administration through Space Act Agreement 34369 with the University of Wyoming. We gratefully acknowledge the assistance of the 14- by 22-Foot Subsonic Tunnel facility staff in conducting these experiments.

References

- [1] Jones, G. W., Jr, and Farmer, M. G., "Wind-tunnel Studies of Ground-wind Loads on Saturn Launch Vehicles." *Journal of Spacecraft and Rockets*, Vol. 4, No. 2, 1967, pp. 219–223.
- [2] Roshko, A., "Experiments on the Flow Past a Circular Cylinder at Very High Reynolds Number," *Journal of Fluid Mechanics*, Vol. 10, No. 3, 1961, pp. 345–356.
- [3] Achenbach, E., "Distribution of Local Pressure and Skin Friction around a Circular Cylinder in Cross-Flow up to $Re = 5 \times 10^6$," *Journal of Fluid Mechanics*, Vol. 34, No. 4, 1968, pp. 625–639.
- [4] Mackey, A. C., and Schwartz, R. D., "Apollo Experience Report-The Development Of Design-Loads Criteria, Methods, And Operational And Midboost Conditions Procedures For Prelaunch, Lift-Off, And Midboost Conditions," NASA TN d-7373, National Aeronautics and Space Administration, 1973.
- [5] Chan, D. T., Paulson, J. W., Shea, P. R., Toro, K. G., Parker, P. A., and Commo, S. A., "Aerodynamic Characterization and Improved Testing Methods for the Space Launch System Liftoff and Transition Environment," *AIAA Aviation 2019 Forum*, AIAA Paper 2019-3398, 2019.
- [6] Pinier, J. T., Herron, A., and Gomez, R. J., "Advances in the Characterization of NASA's Space Launch System Aerodynamic Environments," *AIAA Aviation 2019 Forum*, AIAA Paper 2019-3397, 2019.
- [7] Shea, P. R., Pinier, J. T., Houlden, H., Favaregh, A., Hemsch, M. J., Dalle, D. J., Rogers, S. E., Meeroff, J., and Lee, H. C., "Ascent Aerodynamic Force and Moment Database Development for the Space Launch System," *AIAA Aviation 2019 Forum*, AIAA Paper 2019-3298, 2019.
- [8] Anonymous, "Space Launch System Lift Capabilities," https://www.nasa.gov/sites/default/files/atoms/files/sls_lift_capabilities_configurations_04292020_woleo.pdf, 2020. Accessed October 26, 2021.
- [9] Nikoueeyan, P., Hind, M., Strike, J. A., Perry, M. C., Wimpenny, B., Mears, L. J., Shea, P. R., Collins, J. G., Walker, M. A., Pinier, J. T., and Naughton, J. W., "Evaluating the Utility of Pressure Scanners for Unsteady Pressure Measurements in Wind Tunnel Characterization of the Space Launch System," *AIAA Aviation 2022*, 2022.
- [10] Whitmore, S. A., Lindsey, W. T., Curry, R. E., and Gilyard, G. B., "Experimental Characterization of the Effects of Pneumatic Tubing on Unsteady Pressure Measurements," NASA TM 4171, National Aeronautics and Space Administration, 1990.
- [11] Whitmore, S. A., and Leondes, C. T., "Pneumatic Distortion Compensation for Aircraft Surface Pressure Sensing Devices," *Journal of Aircraft*, Vol. 28, No. 12, 1991, pp. 828–836.

- [12] Whitmore, S. A., and Fox, B., “Improved Accuracy, Second-Order Response Model for Pressure Sensing Systems,” *Journal of Aircraft*, Vol. 46, No. 2, 2009, pp. 491–500.
- [13] Whitmore, S. A., and Wilson, M. D., “Wiener Deconvolution for Reconstruction of Pneumatically Attenuated Pressure Signals,” *AIAA Journal*, Vol. 49, No. 5, 2011, pp. 890–897.
- [14] Strike, J., Hind, M., Saini, M., Naughton, J. W., Wilson, M., and Whitmore, S. A., “Unsteady Surface Pressure Reconstruction on an Oscillating Airfoil Using the Wiener Deconvolution Method,” *27th AIAA Aerodynamic Measurement Technology and Ground Testing Conference*, 2010, p. 4799.
- [15] Nikoueeyan, P., Hind, M., Strike, J., Singh, M., Naughton, J. W., Keeter, S., and Dahland, M., “Characterization of Unsteady Pressures on a Blunt Trailing Edge Using a Direct-Mount Pressure Scanner,” *AIAA SciTech 2019 Forum, AIAA Paper 2019-1827*, 2019, p. 1827.
- [16] Mier, F. A., Nikoueeyan, P., Perry, M., Hind, M., and Naughton, J. W., “Characterizing Remotely Acquired Pressure Measurements from Shock Tube Experiments,” *AIAA SciTech 2022 Forum*, 2022, p. 2172.
- [17] Mears, L. J., Shea, P. R., Collins, J. G., Walker, M. A., Langston, S. L., Pinier, J. T., Nikoueeyan, P., Perry, M., Strike, J., Wimpenny, B., Hind, M., and Naughton, J. W., “Unsteady Pressure Acquisition on the 1.75% Scale SLS Block 1B Cargo Liftoff Configuration,” NASA TM-20220002633, National Aeronautics and Space Administration, 2022.
- [18] Zdravkovich, M. M., *Flow Around Circular Cylinders, Volume 1: Fundamentals*, Oxford University Press, Oxford, 1997.
- [19] Szechenyi, E., “Supercritical Reynolds Number Simulation for Two-Dimensional Flow Over Circular Cylinders,” *Journal of Fluid Mechanics*, Vol. 70, 1975, pp. 529–542.
- [20] Neuhart, D. H., and McGinley, C. B., “Free-Stream Turbulence Intensity in the Langley 14- by 22-Foot Subsonic Tunnel,” NASA TP 213247, National Aeronautics and Space Administration, 2004.
- [21] Bergh, H., and Tijdeman, H., “Theoretical And Experimental Results for the Dynamic Response of Pressure Measuring Systems,” NLR-TR F.238, Amsterdam Nationaal Luchtvaarlaboratorium (National Aeronautical and Astronautical Research Institute), 1965.
- [22] Shih, W. C. L., Wang, C., Coles, D., and Roshko, A., “Experiments on Flow Past Rough Circular Cylinders at Large Reynolds Numbers,” *Journal of Wind Engineering and Industrial Aerodynamics*, Vol. 49, 1993, pp. 351 – 368.
- [23] Neuhart, D. H., Jenkins, L., Choudhari, M., and Khorrami, M., “Measurements of the Flowfield Interaction between Tandem Cylinders,” *15th AIAA/CEAS Aeroacoustics Conference (30th AIAA Aeroacoustics Conference)*, 2009, p. 3275.
- [24] Rossiter, J. E., “Wind-Tunnel Experiments on the Flow over Rectangular Cavities at Subsonic and Transonic Speeds,” R. and M. No. 3438, Aeronautical Research Council, 1964.

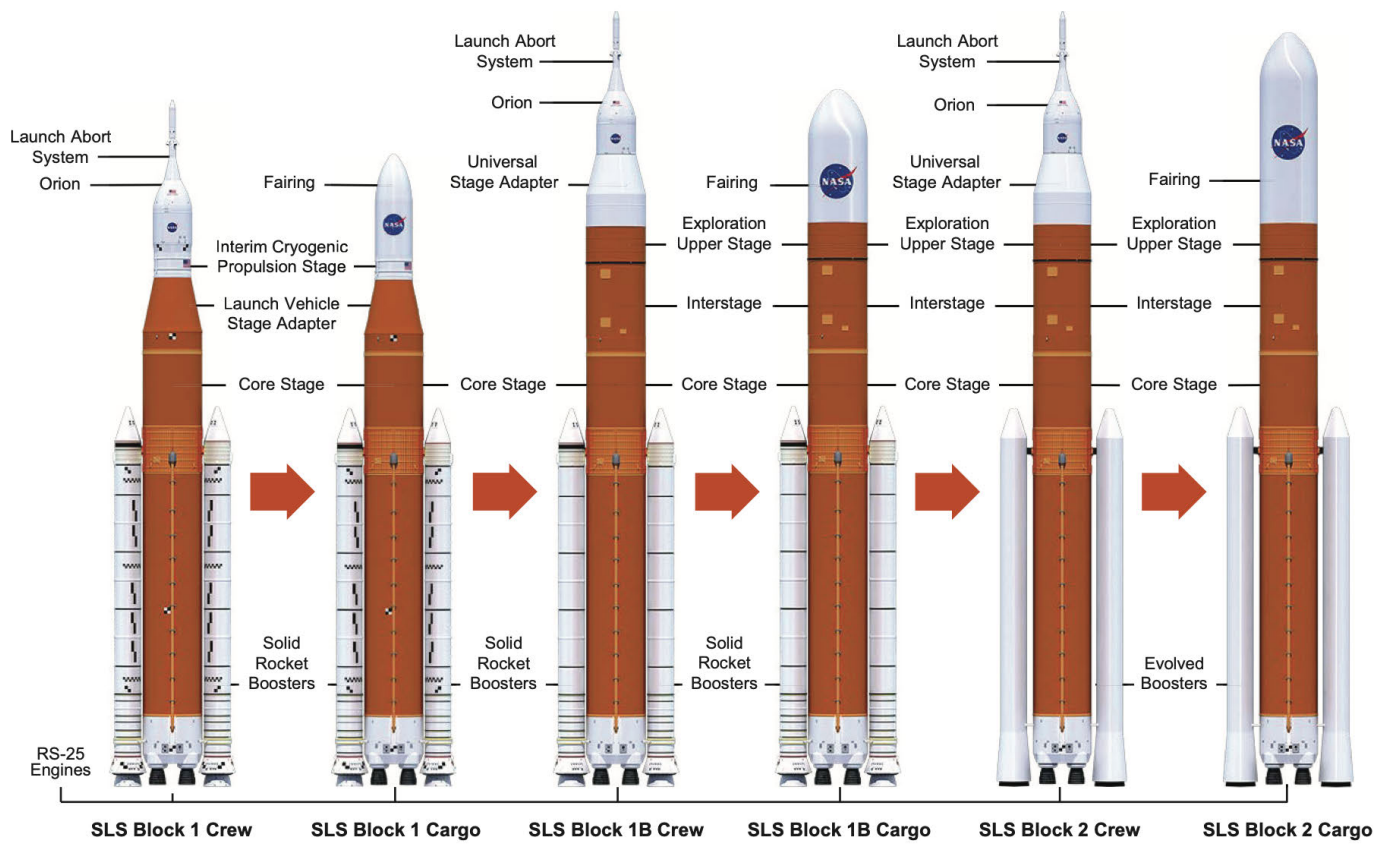


Fig. 1 NASA SLS configurations [8].

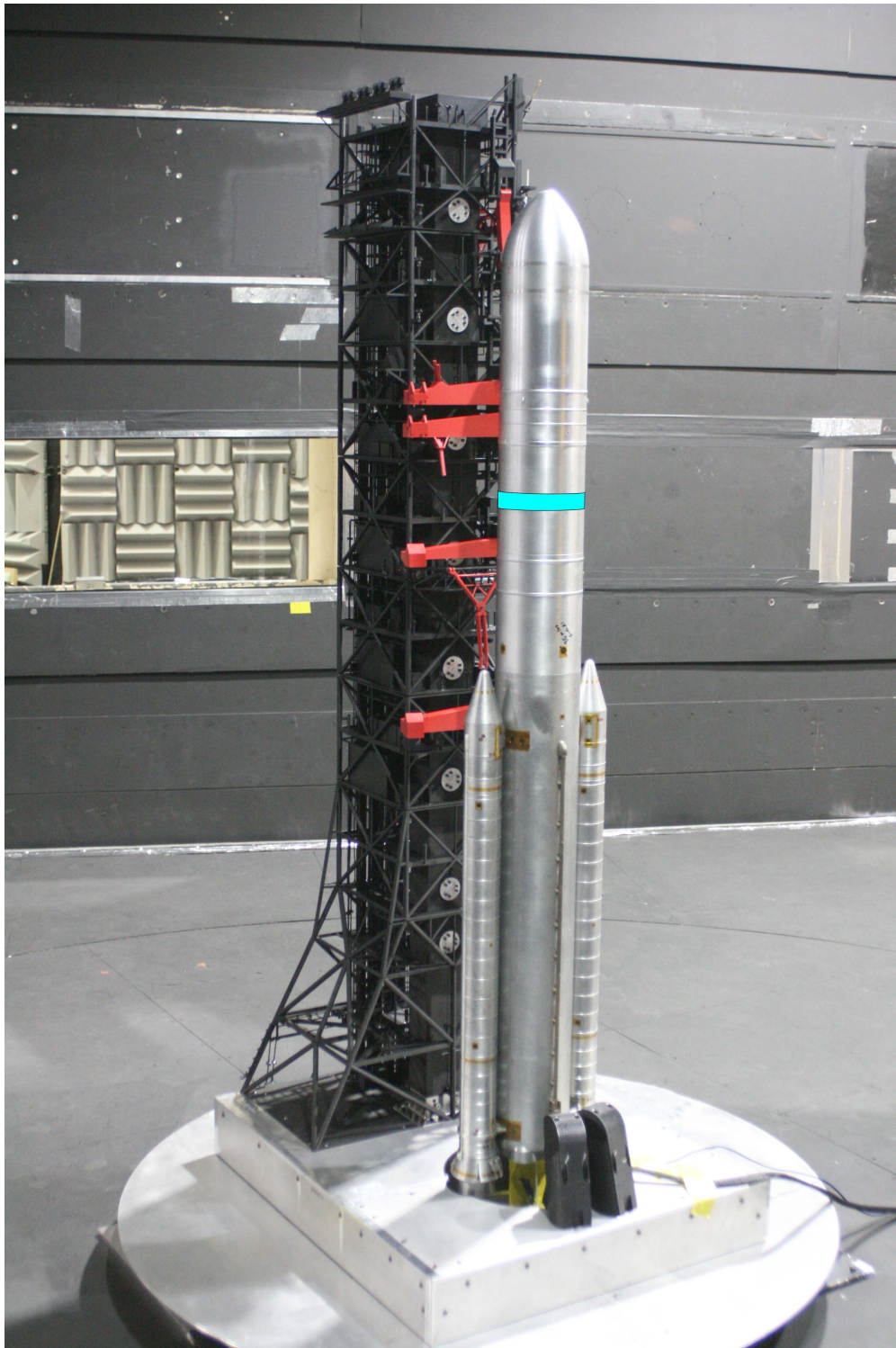
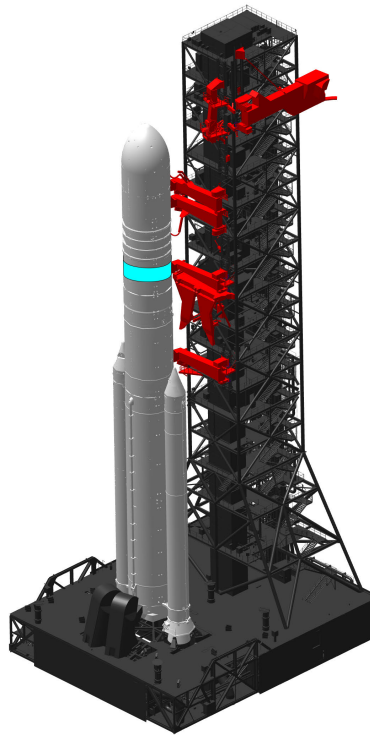
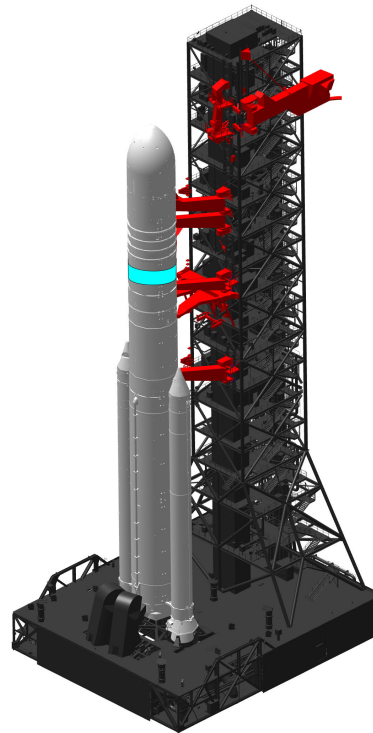


Fig. 2 SLS Block 1B Cargo 1.75%-scale model with mobile launch tower installed in the closed test section of the Langley 14x22 Subsonic Tunnel. The approximate axial location of the pressure tap array on the launch vehicle is indicated in cyan.



(a) C1: umbilicals retracted



(b) C2: umbilicals deployed



(c) C3: vehicle alone

Fig. 3 Model configurations for SLS Block 1B Cargo and ML-2. The approximate axial location of the pressure tap array on the launch vehicle is indicated in cyan.

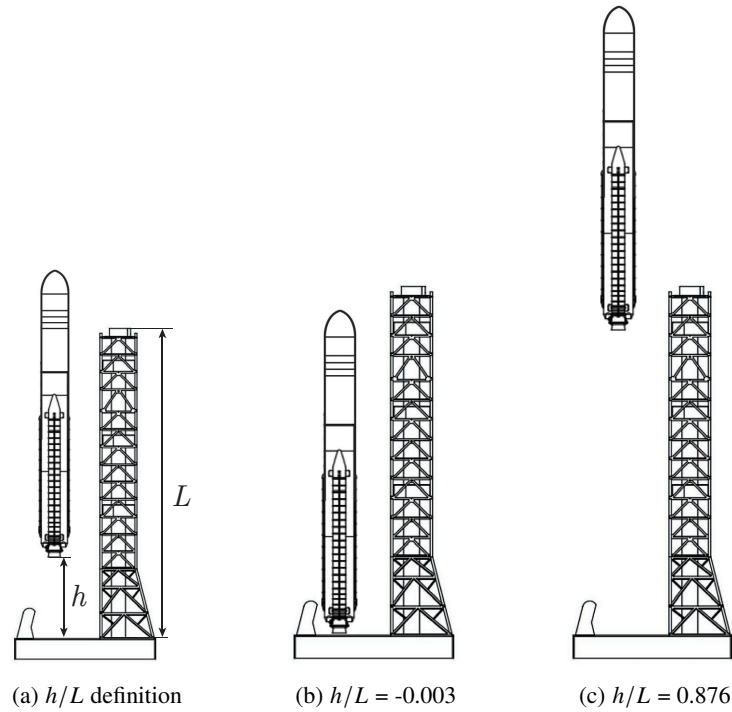


Fig. 4 Launch vehicle elevation with respect to the ML-2 height (h/L) and limiting cases in the present test campaign.

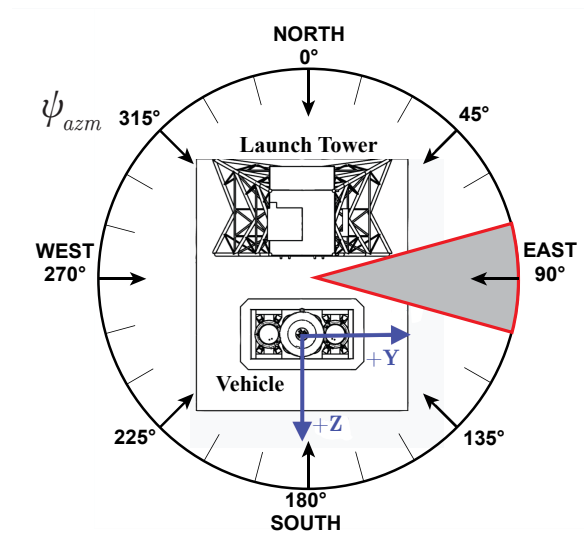


Fig. 5 Top-down view of the model with wind direction ψ_{azm} definition. Angles 80°-100° (gray sector) were not attainable.

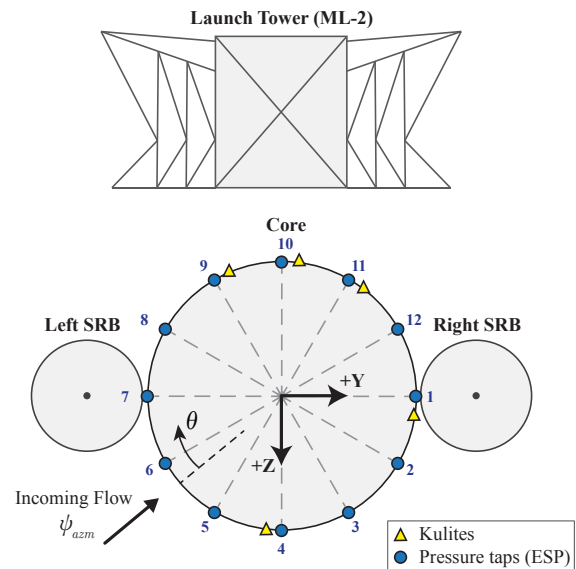


Fig. 6 Top-down view of the model showing the location of 12 pressure taps and 5 surface-mounted Kulites spaced 3° from the taps (ML-2 not to scale).

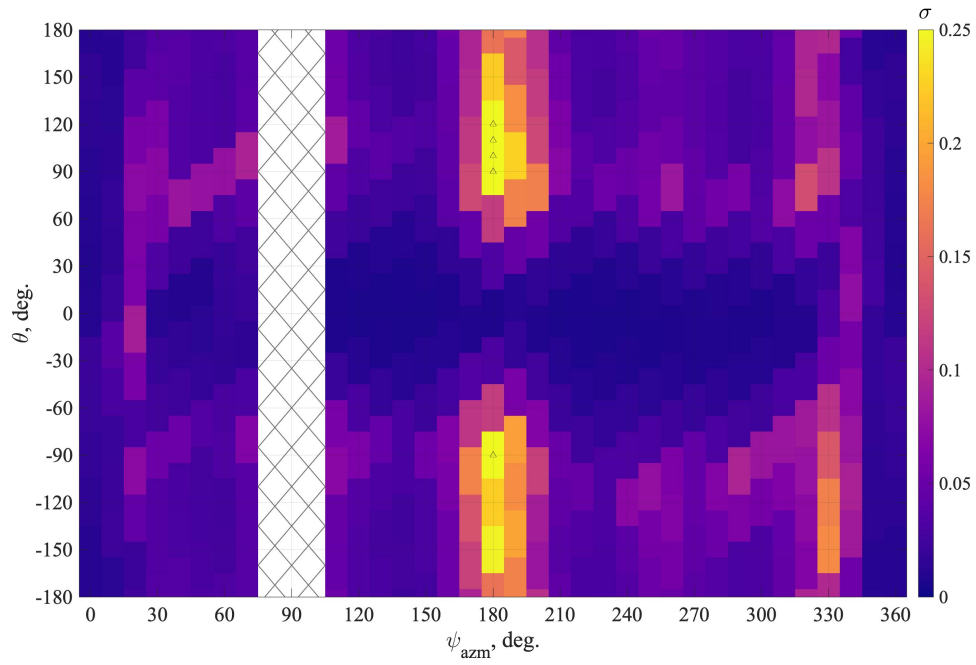


Fig. 7 Pressure intensity (σ) for C1 (with tower and the umbilicals retracted) at $h/L = -0.003$. Black triangles indicate levels of $\sigma > 0.25$.

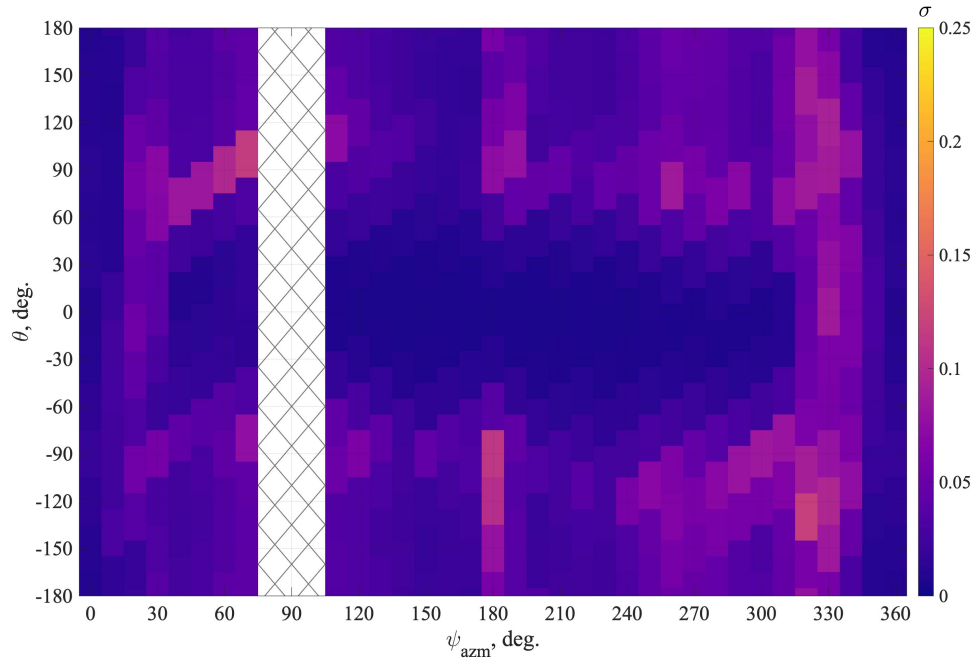


Fig. 8 Pressure intensity (σ) for C1 at $h/L = 0.1$.

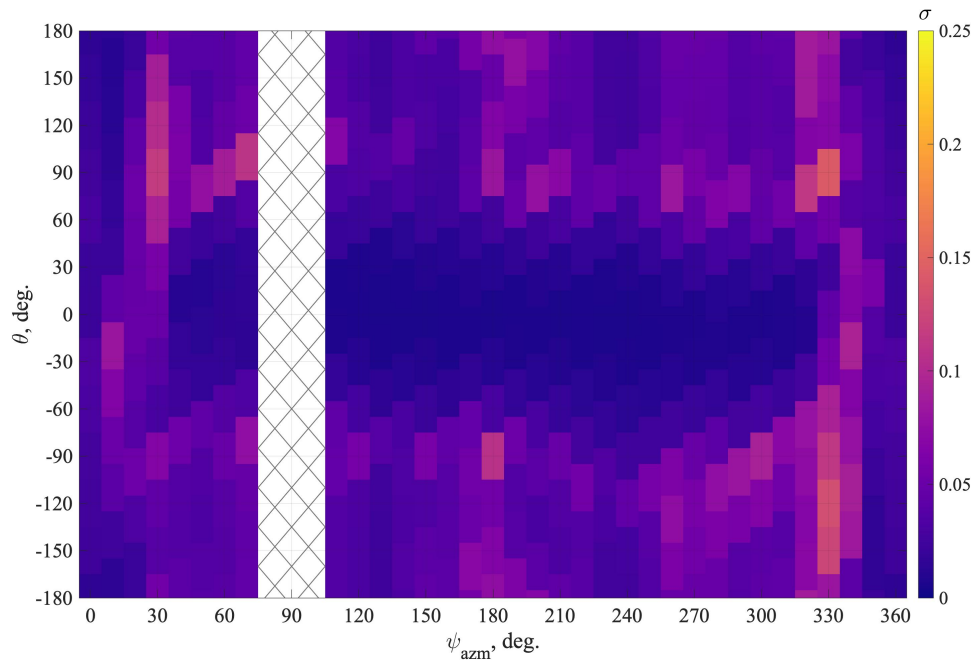


Fig. 9 Pressure intensity (σ) for C1 at $h/L = 0.2$.

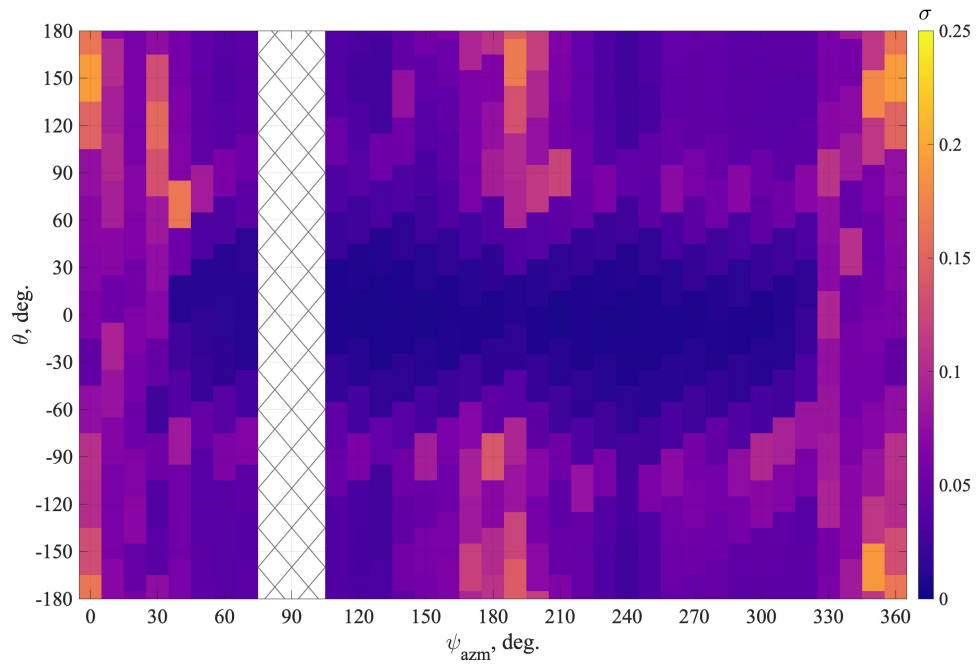


Fig. 10 Pressure intensity (σ) for C1 at $h/L = 0.3$.

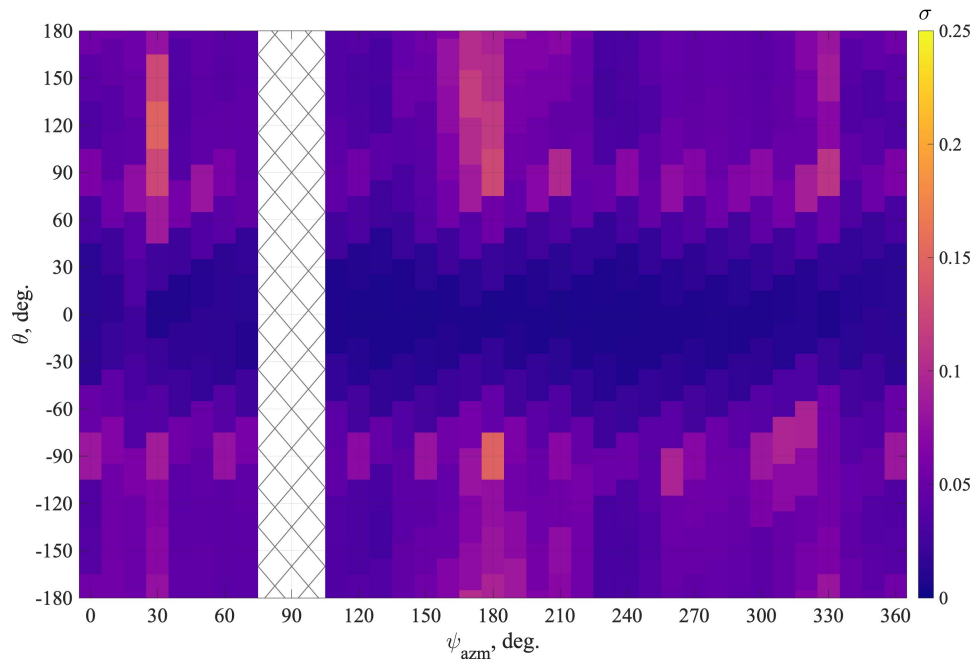


Fig. 11 Pressure intensity (σ) for C1 at $h/L = 0.4$.

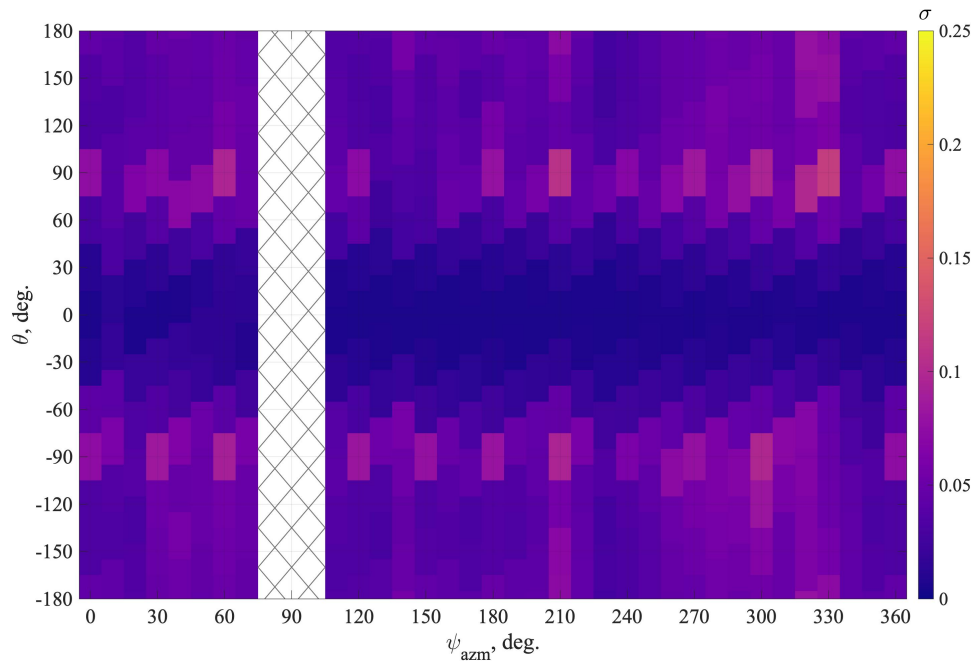


Fig. 12 Pressure intensity (σ) for C1 at $h/L = 0.5$.

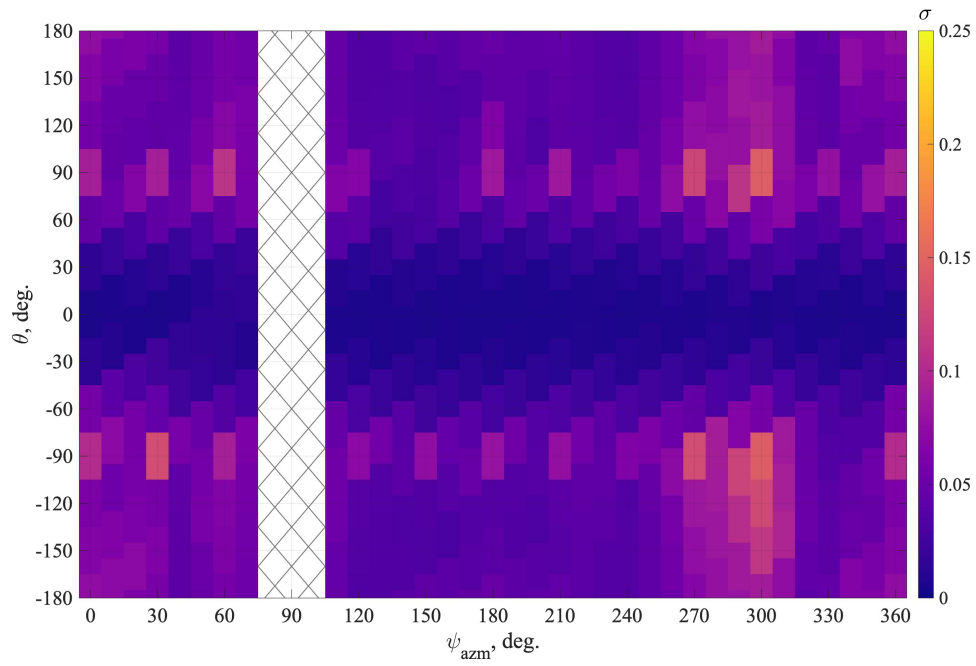


Fig. 13 Pressure intensity (σ) for C1 at $h/L = 0.876$.

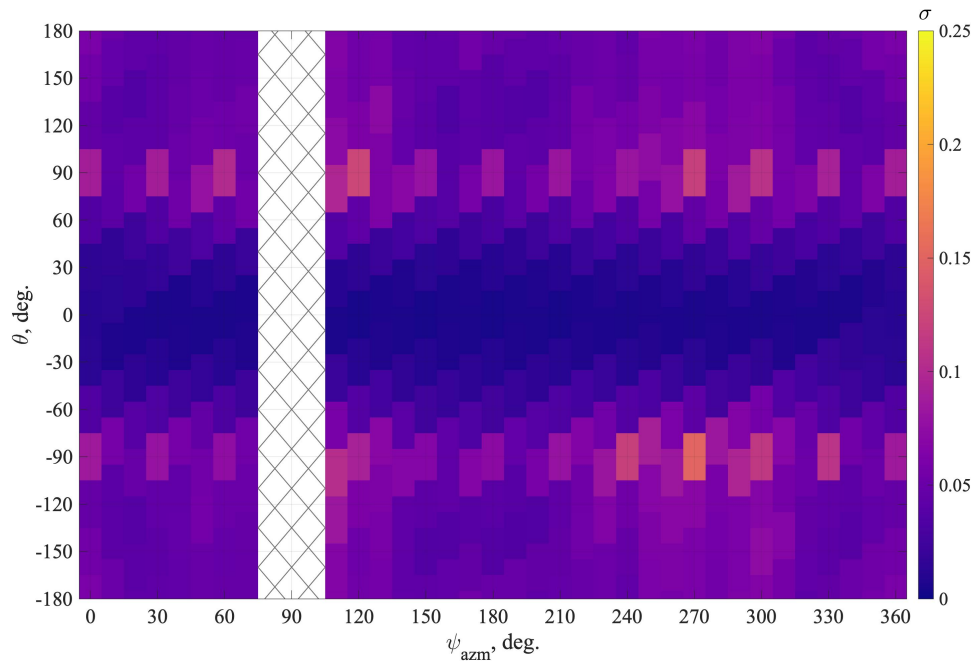


Fig. 14 Pressure intensity (σ) for C3 (no tower) at $h/L = -0.003$.

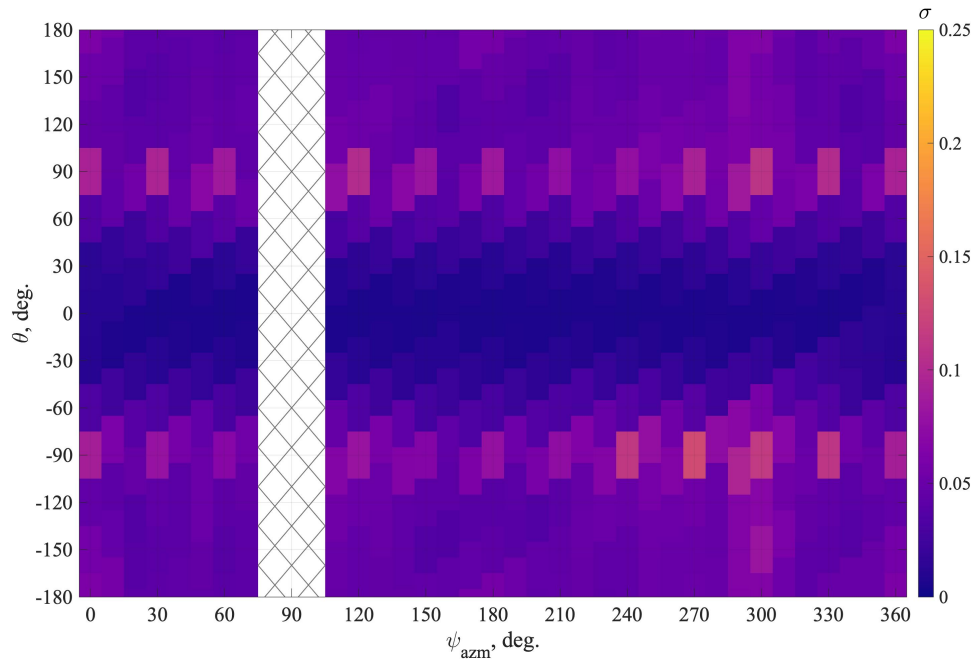


Fig. 15 Pressure intensity (σ) for C3 at $h/L = 0.876$.

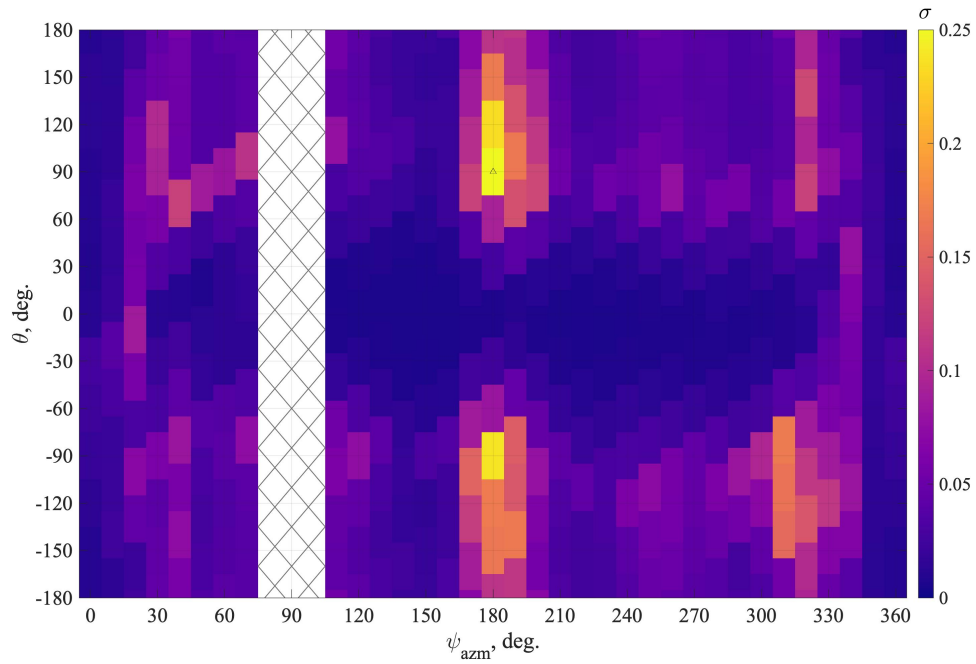


Fig. 16 Pressure intensity (σ) for C2 (with tower and umbilicals deployed) at $h/L = -0.003$. Black triangles indicate levels of $\sigma > 0.25$.

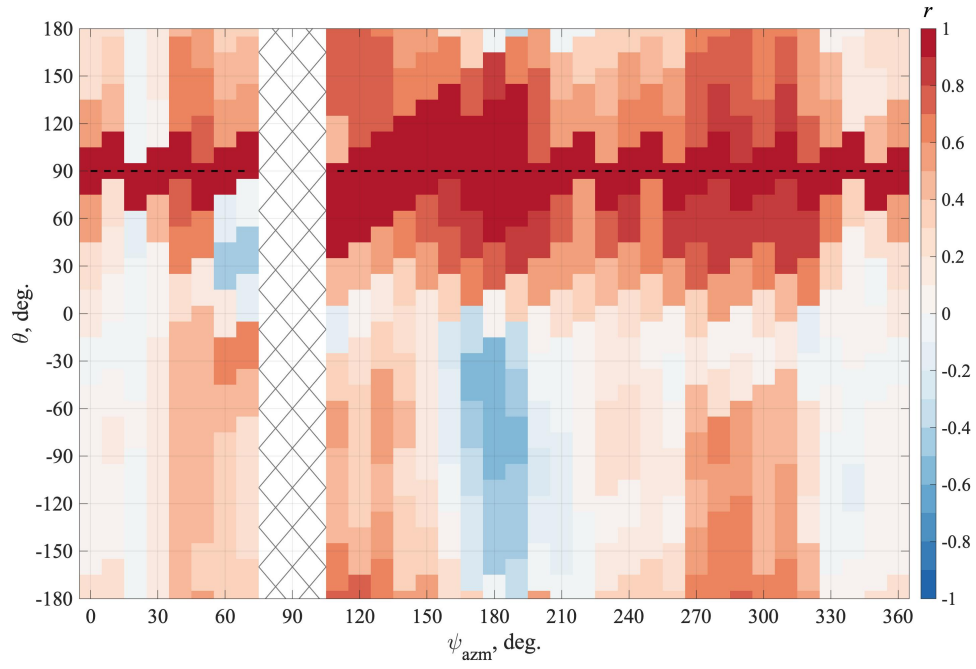


Fig. 17 Correlation coefficient (r) for C1 at $h/L = -0.003$. Reference sensor is located at $\theta = +90^\circ$ (indicated by the black dashed line).

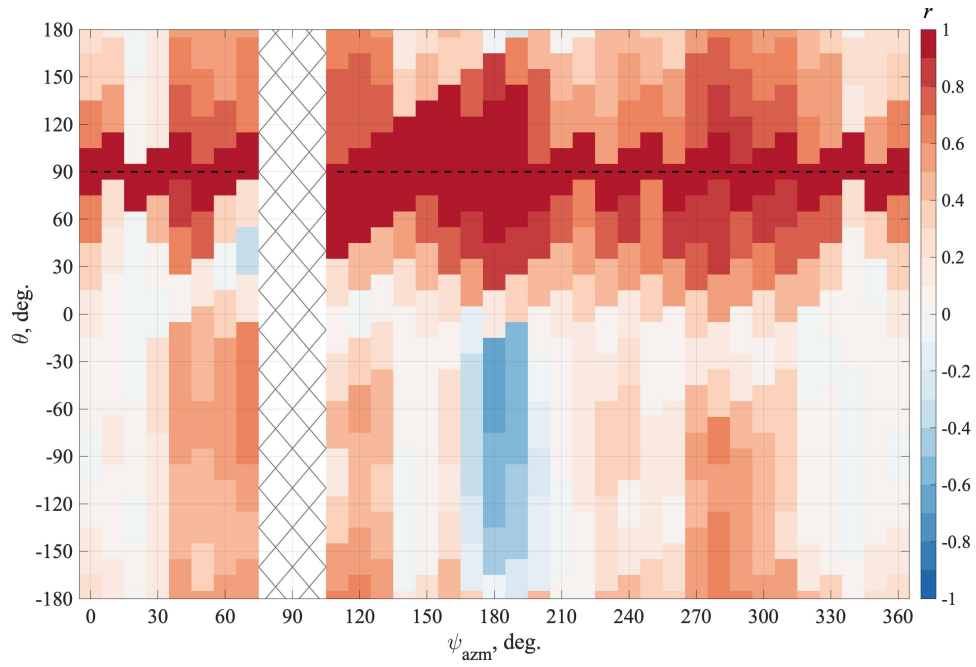


Fig. 18 Correlation coefficient (r) for C2 at $h/L = -0.003$. Reference sensor is located at $\theta = +90^\circ$ (indicated by the black dashed line)

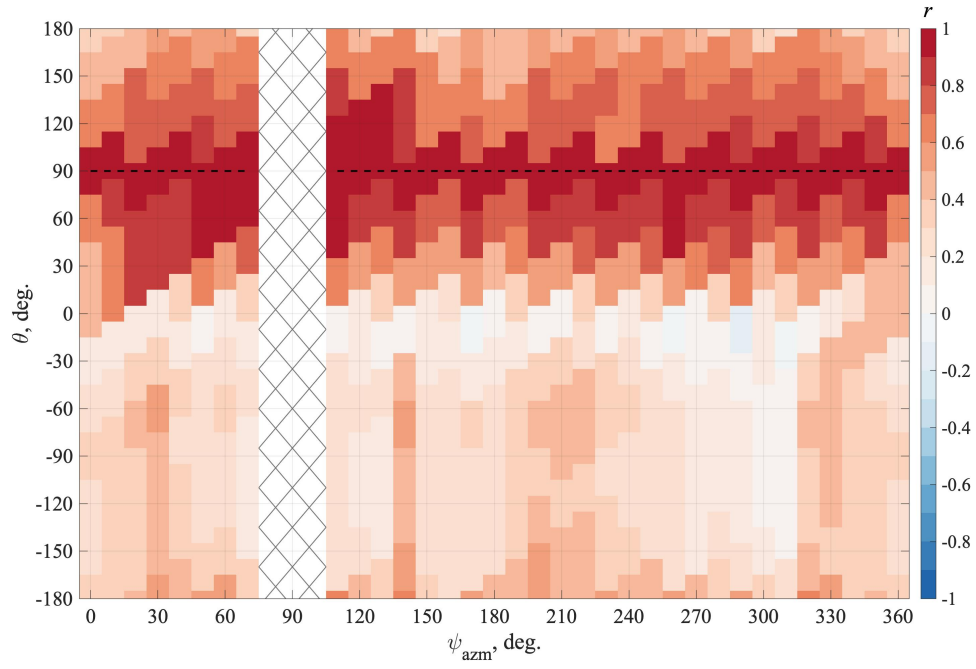


Fig. 19 Correlation coefficient (r) for C3 at $h/L = -0.003$. Reference sensor is located at $\theta = +90^\circ$ (indicated by the black dashed line).

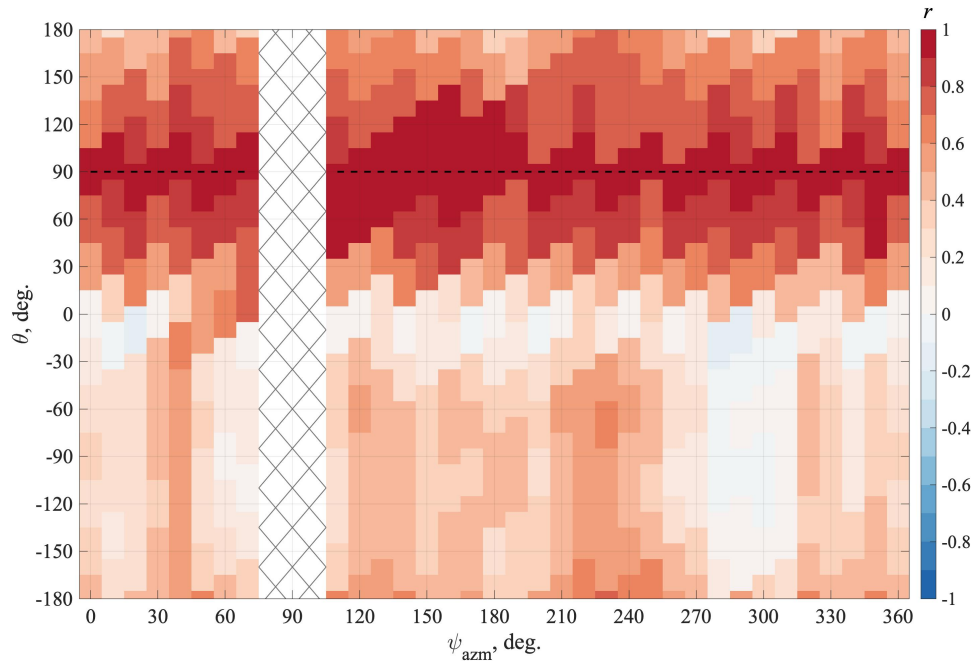


Fig. 20 Correlation coefficient (r) for C1 at $h/L = 0.876$. Reference sensor is located at $\theta = +90^\circ$ (indicated by the black dashed line).

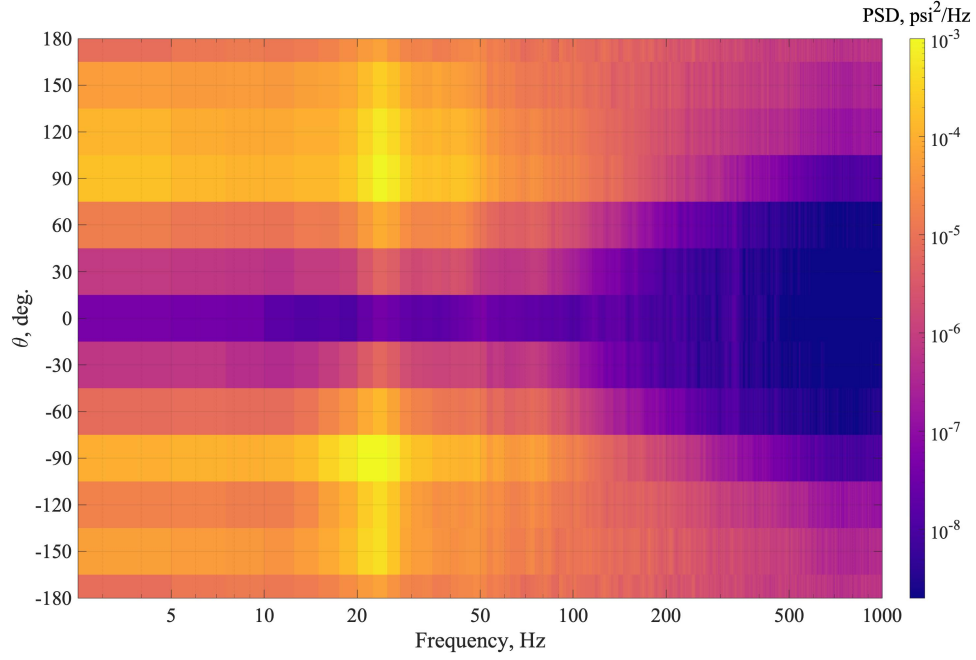


Fig. 21 Distribution of PSD for C1 at $\psi_{azm} = 180^\circ$ and $h/L = -0.003$.

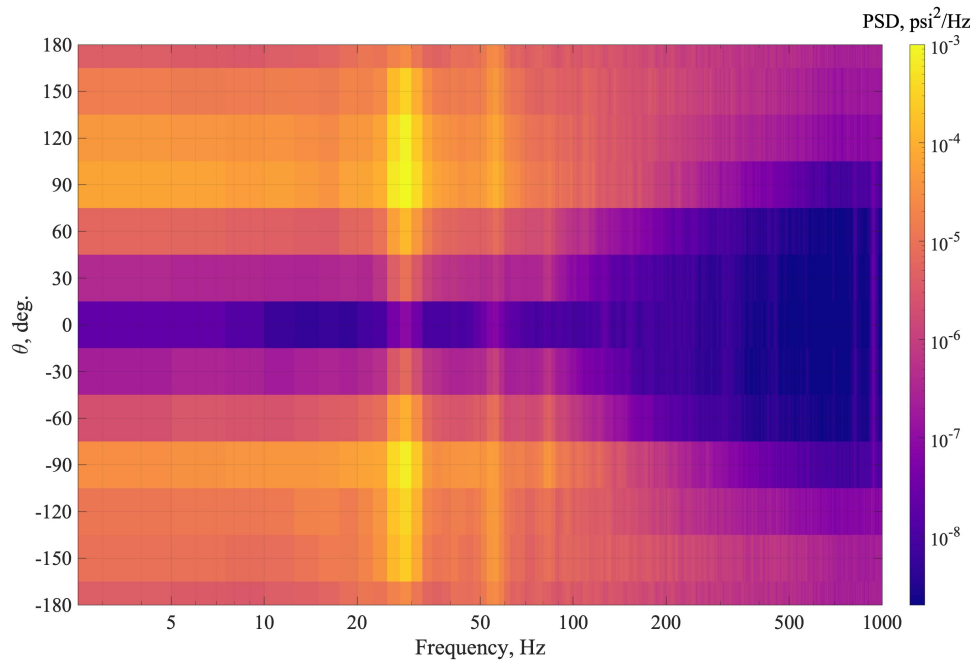


Fig. 22 Distribution of PSD for C2 at $\psi_{azm} = 180^\circ$ and $h/L = -0.003$.

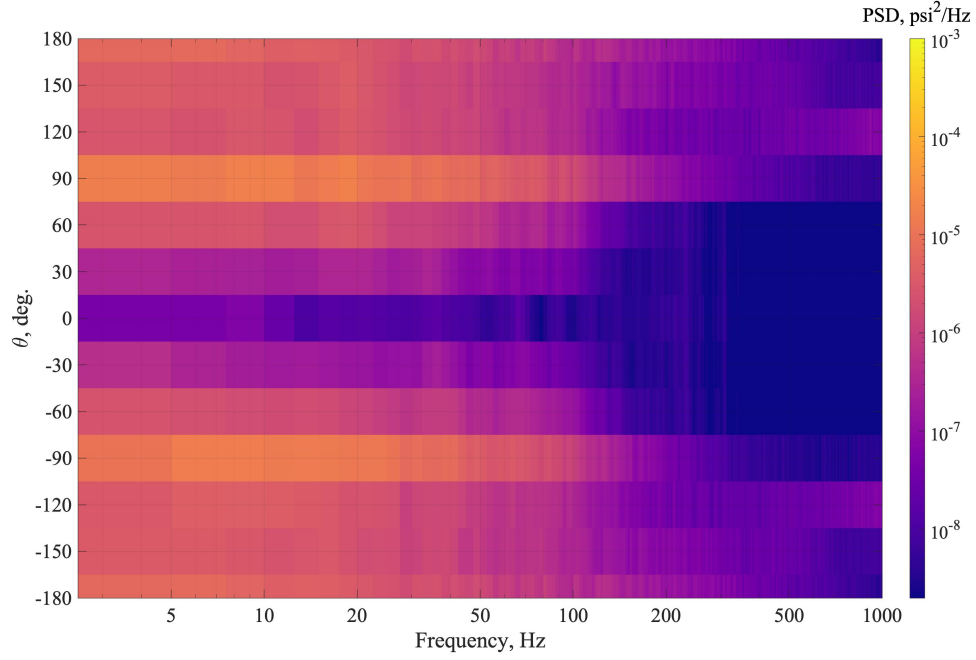


Fig. 23 Distribution of PSD for C3 at $\psi_{azm} = 180^\circ$ and $h/L = -0.003$.

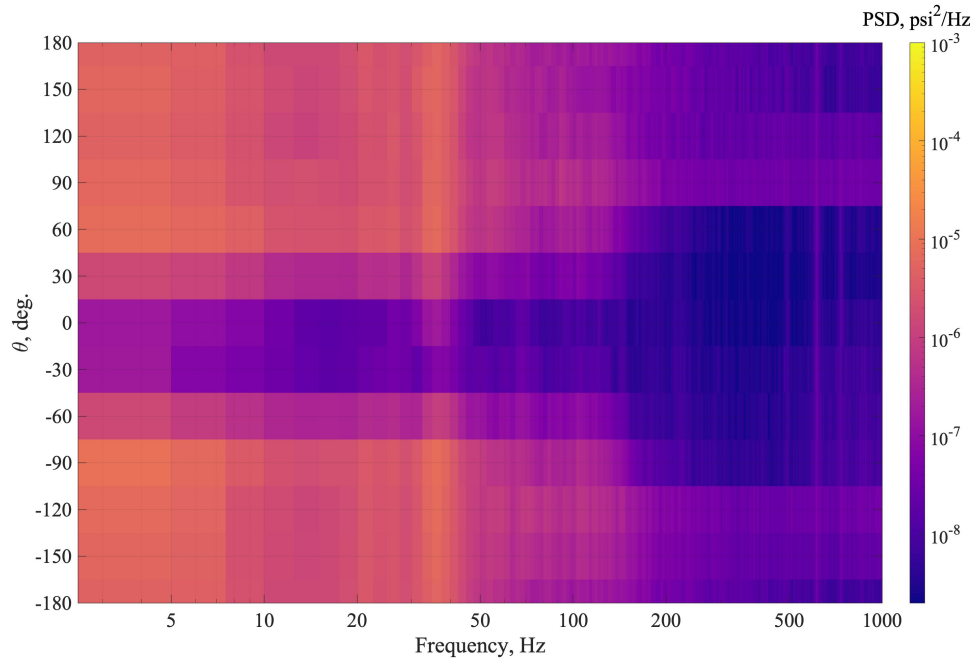


Fig. 24 Distribution of PSD for C1 at $\psi_{azm} = 270^\circ$ and $h/L = -0.003$.

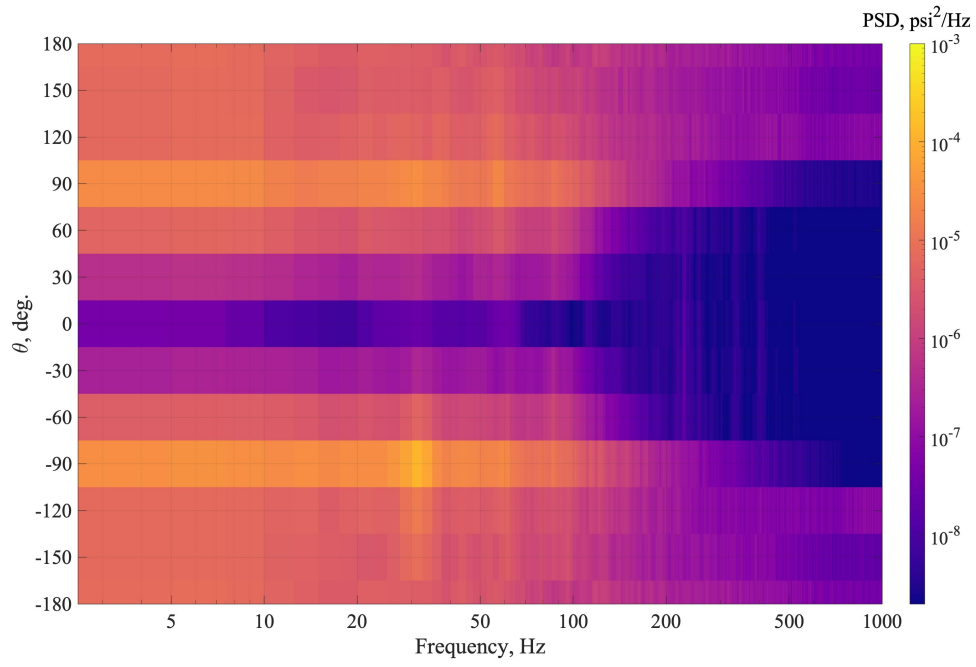


Fig. 25 Distribution of PSD for C3 at $\psi_{azm} = 270^\circ$ and $h/L = -0.003$.

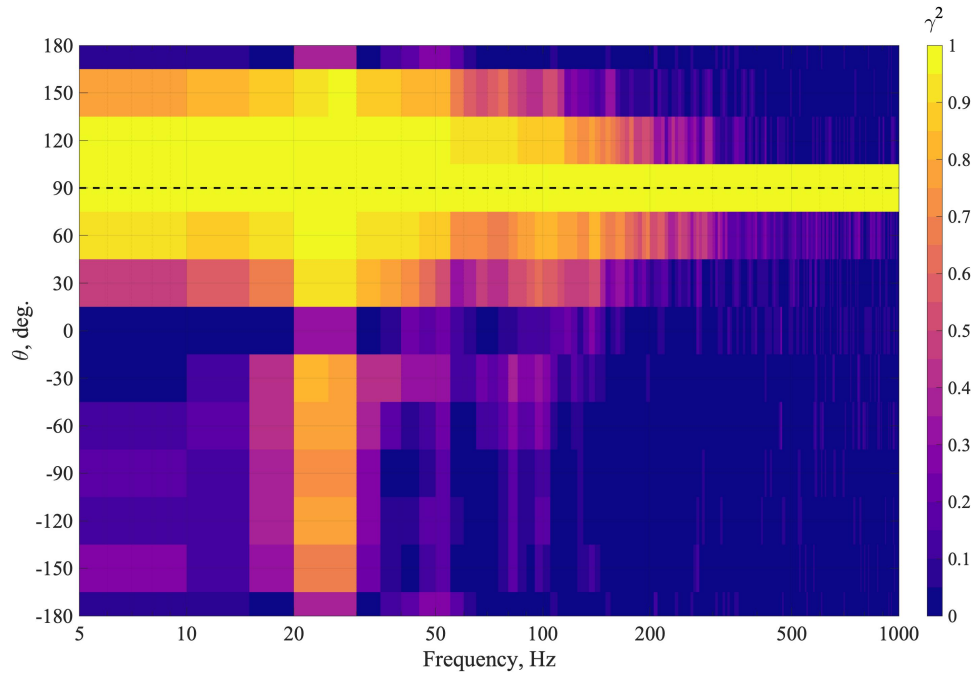


Fig. 26 Distribution of γ^2 for C1 at $\psi_{azm} = 180^\circ$ and $h/L = -0.003$. Reference sensor is located at $\theta = +90^\circ$ (indicated by the black dashed line).

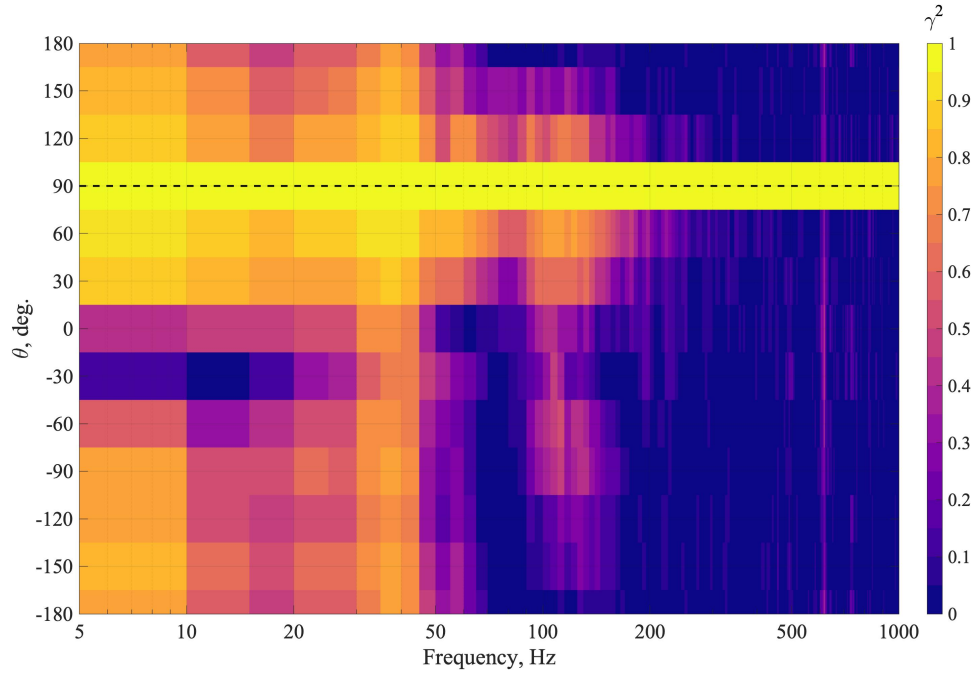


Fig. 27 Distribution of γ^2 for C1 at $\psi_{azm} = 270^\circ$ and $h/L = -0.003$. Reference sensor is located at $\theta = +90^\circ$ (indicated by the black dashed line).

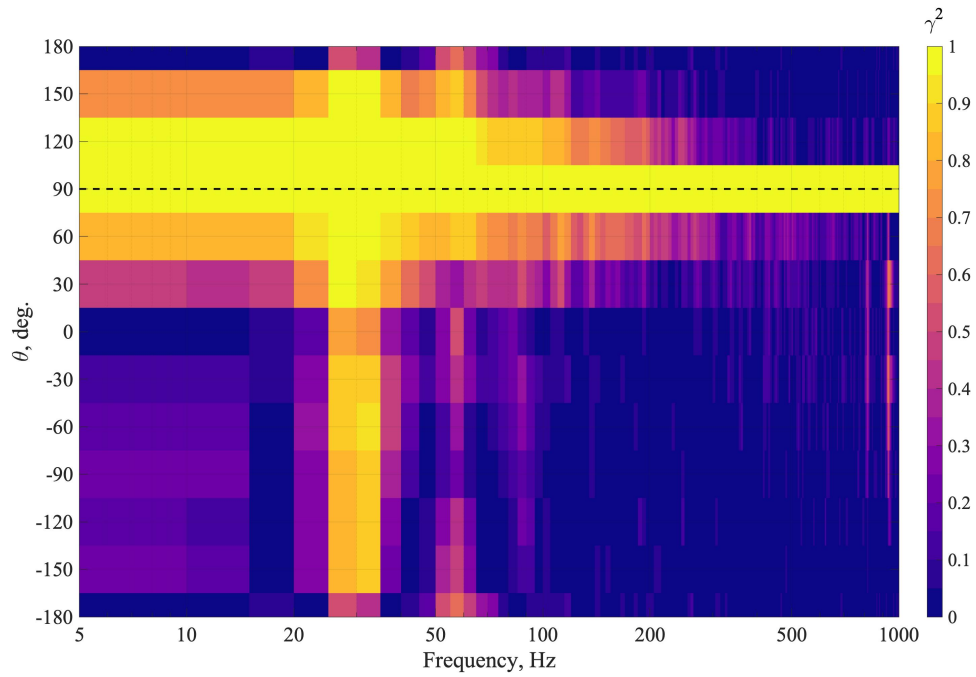


Fig. 28 Distribution of γ^2 for C2 at $\psi_{azm} = 180^\circ$ and $h/L = -0.003$. Reference sensor is located at $\theta = +90^\circ$ (indicated by the black dashed line).

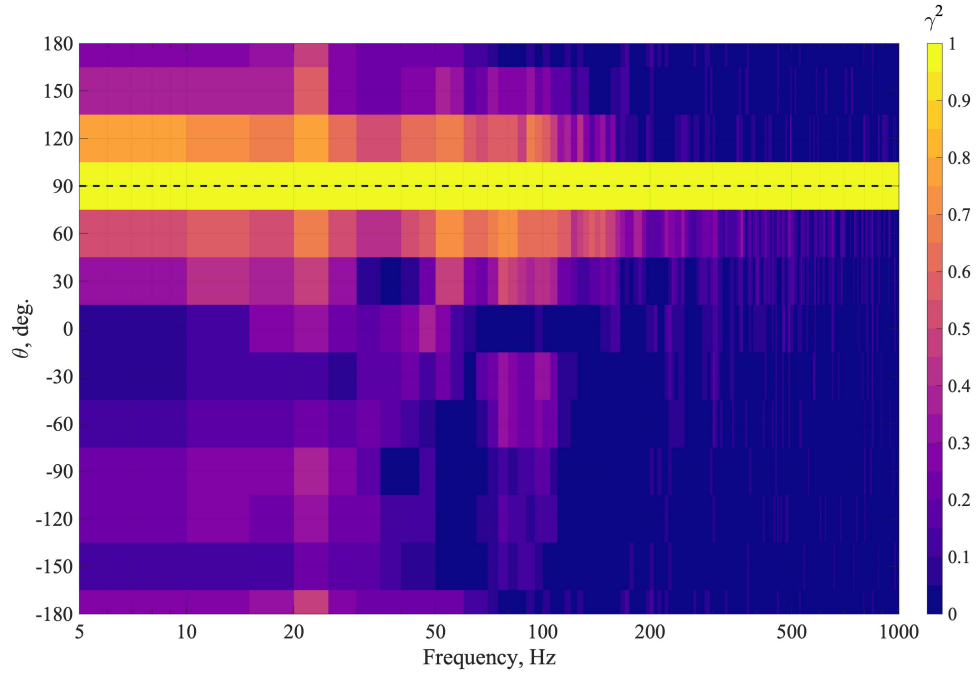


Fig. 29 Distribution of γ^2 for C3 at $\psi_{azm} = 180^\circ$ and $h/L = -0.003$. Reference sensor is located at $\theta = +90^\circ$ (indicated by the black dashed line).

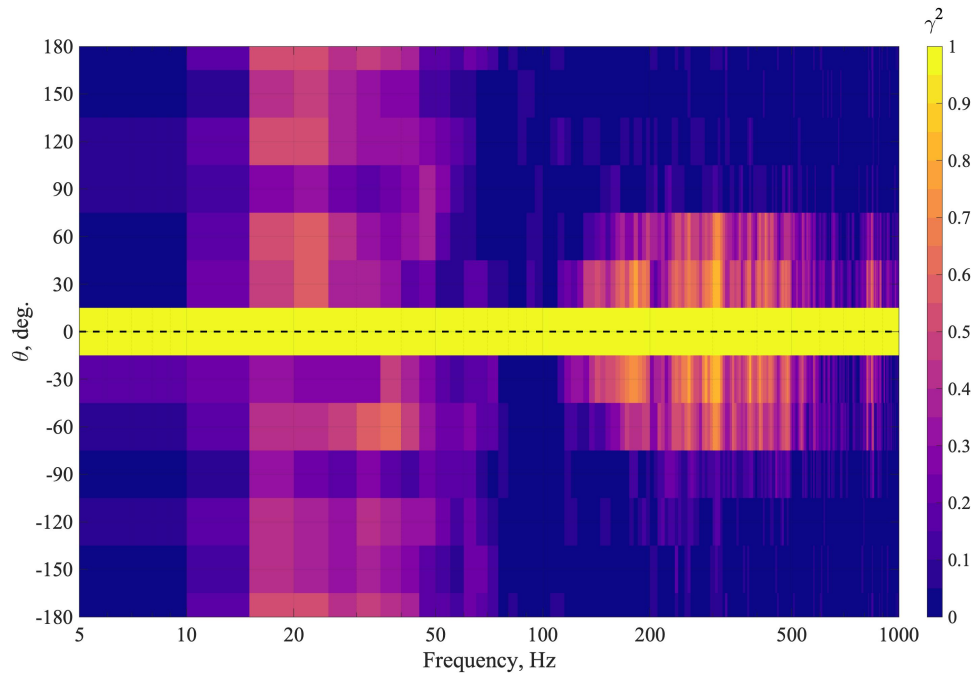


Fig. 30 Distribution of γ^2 for C3 at $\psi_{azm} = 180^\circ$ and $h/L = -0.003$. Reference sensor is located at $\theta = 0^\circ$ (indicated by the black dashed line).

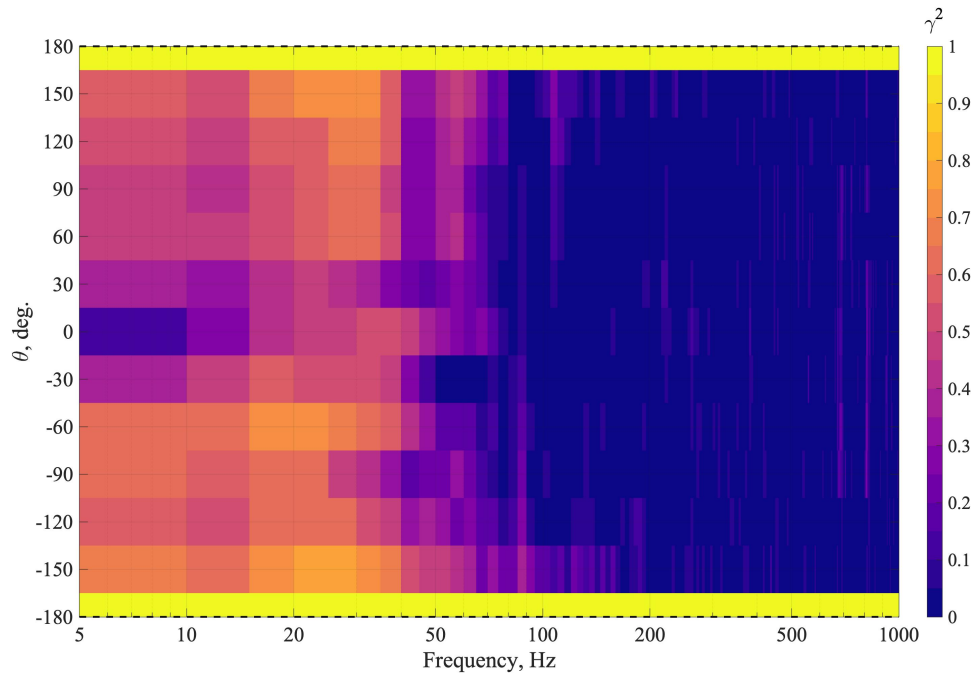


Fig. 31 Distribution of γ^2 for C3 at $\psi_{azm} = 180^\circ$ and $h/L = -0.003$. Reference sensor is located at $\theta = 180^\circ$ (indicated by the black dashed line).

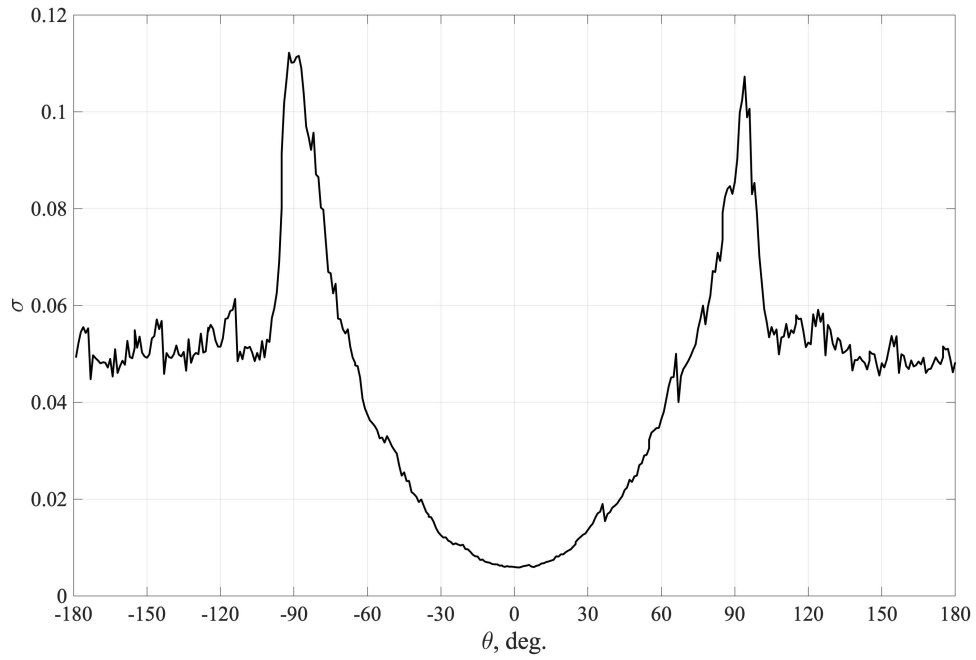


Fig. 32 Distribution of σ for C3 at $\psi_{azm} = 245^\circ$ to 275° and $h/L = 0.5$.

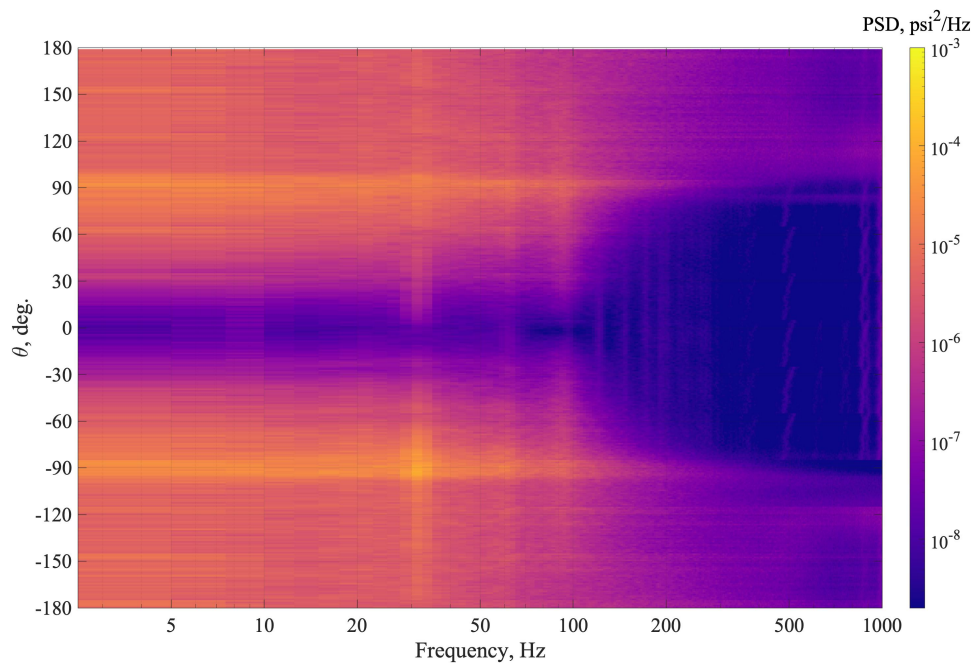


Fig. 33 Distribution of PSD for C3 at $\psi_{azm} = 245^\circ$ to 275° and $h/L = 0.5$.